

# Supercritical CO<sub>2</sub>-Assisted Atomization for Deposition of Cellulose Nanocrystals: An Experimental and Computational Study

**Shadi Shariatnia**

Texas A&M University College Station: Texas A&M University

**Prajesh Jangale**

Texas A&M University College Station: Texas A&M University

**Rohit Mishra**

Texas A&M University College Station: Texas A&M University

**Amir Asadi**

Texas A&M University College Station: Texas A&M University

**Dorin Jarrahbashi** (✉ [djarrahbashi@tamu.edu](mailto:djarrahbashi@tamu.edu))

Texas A and M University: Texas A&M University

---

## Research Article

**Keywords:** Nanoparticle Spray Deposition, Supercritical-Assisted Atomization, Evaporation Induced Nanostructure Fabrication, Cellulose Nanocrystals

**Posted Date:** August 13th, 2021

**DOI:** <https://doi.org/10.21203/rs.3.rs-758403/v1>

**License:**  This work is licensed under a Creative Commons Attribution 4.0 International License.

[Read Full License](#)

---

**Version of Record:** A version of this preprint was published at Cellulose on January 21st, 2022. See the published version at <https://doi.org/10.1007/s10570-021-04368-7>.

1 **Supercritical CO<sub>2</sub>-Assisted Atomization for Deposition of Cellulose Nanocrystals: An**  
2 **Experimental and Computational Study**

3  
4  
5  
6 Shadi Shariatnia <sup>a</sup>, Prajesh Jangale <sup>a</sup>, Rohit Mishra <sup>a</sup>, Amir Asadi <sup>a,b</sup>, Dorrin Jarrahbashi <sup>a\*</sup>

7  
8 <sup>a</sup>J. Mike Walker '66 Department of Mechanical Engineering – Texas A&M University,  
9 College Station, TX 77843, United States

10 <sup>b</sup> Manufacturing and Mechanical Engineering Technology – Department of Engineering  
11 Technology and Industrial Distribution – Texas A&M University, College Station, TX 77843,  
12 United States

13  
14  
15  
16  
17  
18  
19  
20  
21  
22  
23  
24  
25  
26  
27  
28 \* Author for Correspondence

29 Prof. Dorrin Jarrahbashi

30 Texas A&M University

31 Department of Mechanical Engineering

32 MEOB 309

33 College Station, TX 77843-3127, USA.

34 Tel: +1 (979)-862-5972

35 [djarrahbashi@tamu.edu](mailto:djarrahbashi@tamu.edu)

41  
42  
43  
44  
45  
46  
47  
48  
49  
50  
51  
52  
53  
54  
55  
56  
57  
58  
59  
60  
61  
62  
63  
64  
65  
66  
67  
68  
69  
70  
71  
72  
73  
74  
75  
76  
77  
78  
79  
80  
81  
82

## Supercritical CO<sub>2</sub>-Assisted Atomization for Deposition of Cellulose Nanocrystals: An Experimental and Computational Study

Shadi Shariatnia, Prajesh Jangale, Rohit Mishra, Amir Asadi, Dorrin Jarrahbashi

### Abstract

Nanoparticle spray deposition finds numerous applications in pharmaceutical, electronics, manufacturing, and energy industries and has shown great promises in engineering the functional properties of the coated parts. However, current spray deposition systems either lack the required precision in controlling the morphology of the deposited nanostructures or do not have the capacity for large-scale deposition applications. In this study, we introduce a novel spray system that uses supercritical CO<sub>2</sub> to assist the atomization process and create uniform micron-size water droplets that are used as cellulose nanocrystal (CNC) carriers. CNCs are selected in this study as they are abundant, possess superior mechanical properties, and contain hydroxyl groups that facilitate interaction with neighboring materials. We fundamentally investigate the effect of different process parameters, such as injection pressure, gas-to-liquid ratio, the axial distance between the nozzle and substrate, and CNC concentration on the final patterns left on the substrate upon evaporation of water droplets. To this end, we show how tuning process parameters control the size of carrier droplets, dynamics of evaporation, and self-assembly of CNCs, which in turn dictate the final architecture of the deposited nanostructures. We will particularly investigate the morphology of the nanostructures deposited after evaporation of micron-size droplets that has not been fully disclosed to date. Different characterization techniques such as laser diffraction, polarized microscopy, and high-resolution profilometry are employed to visualize and quantify the effect of each process parameter. Numerical simulations are employed to inform the design of experiments. Finally, it is shown that the fabricated nanostructures can be engineered based on the size of the carrier droplets controlled by adjusting spray parameters and the concentration of nanoparticles in the injected mixture. Process parameters can be selected such that nanoparticles form a ring, disk, or dome-shaped structure. Moderate operational conditions, simplicity and time efficiency of the process, and use of abundant and biodegradable materials, i.e., water, CNC, and CO<sub>2</sub> promote the scalability and sustainability of this method.

### Keywords

Nanoparticle Spray Deposition, Supercritical-Assisted Atomization, Evaporation Induced Nanostructure Fabrication, Cellulose Nanocrystals

## 83 1. Introduction

84 Deposition of nanoparticles via liquid atomization finds several practical applications in food,  
85 <sup>1-3</sup> drug delivery, <sup>4,5</sup> manufacturing, <sup>6,7</sup> energy, <sup>8-10</sup> electronics, <sup>11,12</sup> and surface coating. <sup>13</sup> Liquid  
86 atomization is referred to as a hydrodynamic process through which a liquid jet injected via a small  
87 nozzle breaks up into several micron-size and submicron droplets upon exposure to the  
88 surrounding fluid and forms a spray. Spray deposition is a simple one-step, safe and low-cost  
89 method for coating large surface areas within few seconds to promote the efficiency and  
90 scalability, while reducing materials usage. In the nanoparticle spray deposition process, a  
91 colloidal suspension is atomized to create droplets containing nanoparticles of interest that  
92 subsequently evaporate and leave the particles on the target surface.

93 Various configurations of thermal sprays, <sup>14-16</sup> electrical sprays, <sup>17,18</sup> and direct-write  
94 deposition <sup>19-22</sup> are among the most common spray deposition methods that have been extensively  
95 studied. Thermal spray systems such as warm, <sup>23,24</sup> plasma, <sup>25-27</sup> and electro sprays <sup>28,29</sup> use a heat  
96 source, either through a chemical reaction, plasma discharge, or electricity to melt the feedstock  
97 material and spray it on a substrate using a high-speed jet. Cold spray systems where solid powders  
98 (rather than a melted material) are accelerated in a de Laval nozzle towards the substrate, fall under  
99 the thermal spray category. <sup>15</sup> Due to the harsh conditions in these sprays, coatings and substrates  
100 are limited to materials that can withstand large impact forces and are compatible with high  
101 temperature (and/or temperature gradients). <sup>30</sup> Metals and metallic alloys, ceramics, glasses,  
102 polymers, and plastics are commonly used as the coating material in such systems. <sup>15</sup> These  
103 coatings are often utilized to prevent chemical and mechanical damage to different structures  
104 depending on the functionality of the part. <sup>31</sup> Thermal sprays are cost effective and can cover large  
105 surface areas in a short period of time with a thickness that can range from ~20 microns to several  
106 millimeters. <sup>32</sup> However, thermal methods lack the precision needed for coatings layers with a few  
107 nanometer thicknesses, and they do not provide any control over the formation and final  
108 morphology of the deposited nanostructures. <sup>29</sup>

109 Direct-write deposition techniques on the other hand, e.g. inkjet and aerosol jet printing,  
110 precisely control the deposition of colloidal droplets and formation of nanostructures on a targeted  
111 location. <sup>19,33</sup> These methods find numerous applications in electronics <sup>34-40</sup> and life sciences, <sup>41-43</sup>  
112 with a plethora of research focused on developing customized inks for printing different materials.  
113 <sup>44-47</sup> Upon deposition on the substrate, the contact line of the ink droplets pins to the substrate. As  
114 the droplet evaporation proceeds, the contact angle between the droplet and substrate decreases.  
115 As a result, a capillary flow from the center of the droplet towards the pinned contact line initiates  
116 to compensate the liquid mass loss at the droplet's periphery. <sup>48</sup> This flow drags the particles and  
117 accumulates them along the edge of the droplet leaving a ring-shaped trace of particles on the  
118 substrate. <sup>49</sup> This phenomenon is known as the coffee ring effect (CRE) that can be exploited or  
119 suppressed to enforce a specific nanoparticle pattern on the substrate depending on the application.  
120 <sup>48</sup> Suppression of the CRE in direct writing methods requires costly and multi-step processes such  
121 as the use of flammable, toxic, and hazardous surfactants to the solvent, <sup>50-52</sup> physical and chemical  
122 modification of the substrate, <sup>53,54</sup> and imposing external electrical, magnetic, or acoustic forces.

123 <sup>55-57</sup> Inkjet printing is limited to deposition of a single or a few droplets at a time that covers a small  
124 surface area limiting the scalability of this technique. In addition, since the process parameters are  
125 set prior to print, achieving thickness and material variability, requires multiple rounds of  
126 deposition or using multiple print heads. <sup>58, 59</sup>

127 There are also several high-throughput spray-based techniques to create and release  
128 nanoparticles through atomization of colloidal solutions, such as spray pyrolysis <sup>60</sup> and spray  
129 drying <sup>61</sup> widely used in pharmaceutical and food industries. <sup>62-64</sup> Their adoption is owed to the  
130 compatibility of these techniques with a large variety of materials. In our previous study, the  
131 superiority of spray deposition of cellulose nanocrystals over other conventional coating methods  
132 (i.e., dip-coating) was fully studied. <sup>65</sup> However, due to the inherent uncertainties, randomness,  
133 and wide size distribution of droplets created by atomization, these systems lack the precision and  
134 control over the formation and homogeneity of the produced nanoparticles. <sup>66</sup> Aerosol jet printing  
135 utilizes an air-assisted atomization technique for breakup of the liquid jet stream and a specific  
136 directed nozzle to facilitate targeted deposition. <sup>67</sup> This technique is faster than inkjet printing and  
137 is compatible for deposition on any substrate and capable of handling a wide range of materials in  
138 moderate operating conditions (i.e., low temperatures and pressures). <sup>12, 68</sup> It also provides precise  
139 control over the thickness and profile of the material deposition with the first round of spray. <sup>69, 70</sup>  
140 However, aerosol jet printing lacks the capability of large-scale printing/deposition. <sup>71, 72</sup> The  
141 internal design of the nozzle that directly affects the quality and dimensional resolution of the print  
142 is very complicated and is not suitable for printing single dots or square-shaped geometries. <sup>59, 73</sup>  
143 Other limitations of this method include low solubility of particles in the solvent and lack of control  
144 over droplet sizes. <sup>74, 75</sup>

145 To overcome these limitations, supercritical-assisted atomization (SAA) has been introduced  
146 as a method that utilizes a fluid above its thermodynamic critical point to facilitate the atomization  
147 process by enhancing the nanoparticles dissolution in solvents. <sup>76</sup> SAA accelerates liquid  
148 atomization by exploiting the hybrid gas-like and liquid-like properties of supercritical fluids. High  
149 density and high diffusivity along with low viscosity of supercritical fluids enhances the  
150 dissolution of gasses into the injected mixture (comprised of the solvent and nanoparticles) and  
151 reduces the surface tension between the injected liquid and the surrounding gas that both contribute  
152 to an improved atomization process and spray formation. <sup>77, 78</sup> Owing to their high diffusivity,  
153 supercritical fluids highly dissolve in the liquid mixture prior to injection and separate from the  
154 mixture in the form of gas bubbles upon injection into the surrounding environment. The sudden  
155 expansion of these gas bubbles, triggers the breakup of the liquid jet and shatters it into very fine  
156 and highly uniform droplets with a narrow size distribution compared to other spray-based  
157 techniques. <sup>79</sup> Material selection is an important factor in designing the SAA system, especially in  
158 micronization and powder manufacturing applications where solid particles that are dissolved in  
159 the supercritical mixture need to preserve their properties after dissolution. CO<sub>2</sub> is an abundant,  
160 degradable, nontoxic, and nonflammable gas with moderate critical temperature and pressure  
161 (31°C and 7.4 MPa) compared to other fluids, which makes it a viable option for several  
162 applications such as temperature-sensitive materials used in pharmaceutical and biological

163 applications.<sup>80, 81</sup> The high solubility of supercritical CO<sub>2</sub> (SCO<sub>2</sub>) in most organic and inorganic  
164 solvents has made it the supercritical fluid of choice in SAA systems.<sup>82, 83</sup> Sensitivity of mixture  
165 properties to the operational conditions enables the regulation of droplet sizes and the final  
166 morphology of the fabricated particles.<sup>84</sup> Although SAA provides great control over process  
167 parameters, it is limited to solely manufacturing micro/nanoparticles that are collected in a  
168 precipitator in the form of dry powder after atomization.

169 An important application of SAA is the direct deposition of nanoparticle-carrier droplets  
170 resulting from atomization of nano-colloidal suspensions exposed to SCO<sub>2</sub> and exploiting that  
171 process to engineer the nanostructures on a substrate. However, due to complex underlying  
172 atomization mechanisms in SAA, this potentially important application has not been fully explored  
173 in the literature to date. This knowledge gap motivated the current study where we have designed  
174 and built a novel SAA system to atomize aqueous Cellulose nanocrystal (CNCs) suspension and  
175 deposit the droplets containing CNC on a solid substrate to fabricate nanostructures with controlled  
176 size and morphology. In our previous study, we experimentally studied the effect of a wide range  
177 of process parameters such as GLR, injection pressure, and axial distance from the injection orifice  
178 on the breakup and final droplet size in the absence of nanoparticles<sup>85</sup>. In this study, we utilize  
179 SAA as a new large-scale delivery method for depositing CNCs and controlling the fabrication of  
180 nanostructures on solid substrates. The proposed spray deposition technique can seamlessly be  
181 adopted for several practical applications involving CNCs and other nanoparticles. The main  
182 objective of this study is to (1) understand the effect of spray parameters and colloidal suspension  
183 properties on the shape of the nanostructures formed on the substrate after droplet evaporation,  
184 and (2) use this knowledge to effectively control and tailor the architecture of deposited  
185 nanostructures.

186 We adopted CNC in this study as it forms a stable dispersion in water and possesses unique  
187 mechanical and chemical properties that make it appealing for a variety of applications, from 3D  
188 printing<sup>7</sup> and manufacturing,<sup>86-88</sup> to drug delivery<sup>89</sup> and electronics.<sup>90</sup> CNCs with linear chain  
189 glucose units (C<sub>6</sub>H<sub>10</sub>O<sub>5</sub>) are abundant, non-toxic, and biodegradable spindle-shaped nanoparticles  
190 obtained from plants, algae, bacteria, and marine animals.<sup>91, 73</sup> CNC contains accessible hydroxyl  
191 groups on its surface that makes it suitable for chemical modification.<sup>92</sup> In addition, CNCs possess  
192 unique features such as low density (1.5 g/cm<sup>3</sup>), elastic modulus of 110-220 GPa, tensile strength  
193 of 3-7.5 GPa, high aspect ratio (10-100), and high surface area.<sup>92</sup> Evaporation-induced self-  
194 assembly of aqueous CNC droplets has been widely studied for optical sensing, security labeling,  
195 food, cosmetics, textiles, and art applications.<sup>93-97</sup> However, these studies are focused on  
196 investigating the patterns in a liquid film or a single droplet and involve time and cost-inefficient  
197 lab-scale processes. To this end, we experimentally investigate the effect of different spray  
198 parameters and the concentration of CNC on the mean droplet sizes and the morphology of the  
199 created nanostructure. We have leveraged computational fluid dynamics (CFD) simulations to  
200 obtain the optimum spray parameters, achieve the desired film thickness, and indicate the prime  
201 location for delivery of droplets on the substrate where minimum droplet evaporation and spray  
202 bounce-back occurs. The computational results inform the experimental system design, and thus

203 reduce the trial-and-error process to obtain the optimum deposition outcome with minimum  
204 material waste and ensure system scalability.

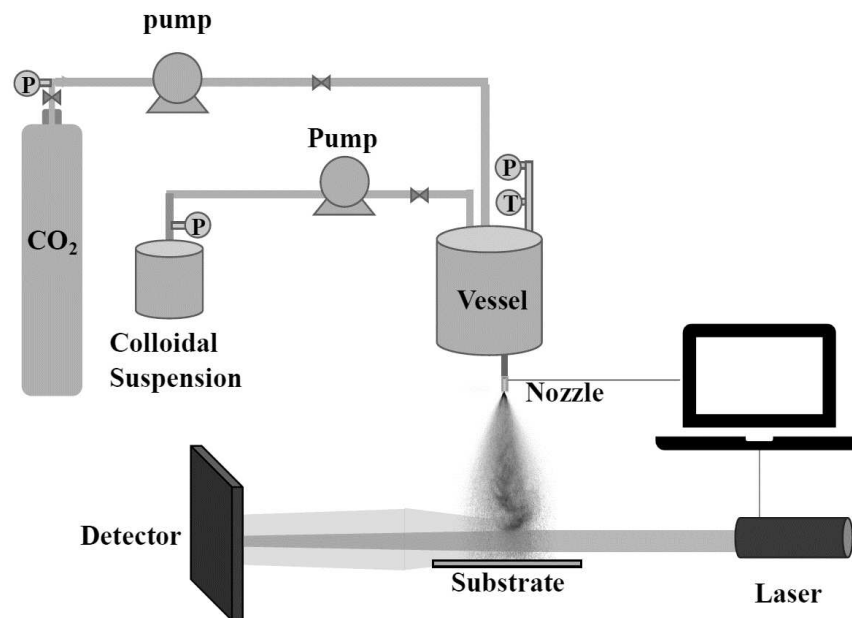
205 The remainder of this paper is structured as follows: the spray deposition setup and materials  
206 selected for this work, as well as the characterization techniques, are described in *Section 2*.  
207 Governing equations and computational methods utilized in simulations are described in *Section*  
208 *3. Results and Discussion* are presented in *Section 4*, where the effects of spray parameters on the  
209 final nanostructures assembled on the substrate are visualized and measured using microscopy and  
210 profilometry. The resulting film thickness and droplet behavior at different spray parameters from  
211 numerical simulations are also presented. The *Conclusions* presented in *Section 5* concludes this  
212 paper.

## 213 2. Experimental Method

### 214 2.1 Spray Setup and Diagnostics

215 **Figure 1** shows a schematic of the experimental setup for SAA spray deposition of CNCs on  
216 a glass substrate. The spray system has two feed lines that deliver CO<sub>2</sub> and the aqueous CNC  
217 suspension to a custom-made pressure vessel. The ternary mixture, i.e., CNC, water, and CO<sub>2</sub>, mix  
218 and reside in the pressure vessel. A pump feeds the colloidal suspension into the pressure vessel,  
219 while another pump connects the CO<sub>2</sub> tank to the pressure vessel. Pressure and temperature are  
220 monitored in multiple locations along the feeding lines and inside the vessel using several pressure  
221 gauges and thermometers. The mixture is then injected into the ambient atmospheric air towards a  
222 glass substrate (VWR, micro cover glass No. 1.5). The internal geometry of the nozzle is a straight,  
223 circular cylinder with an actuator.

224



225

226

227

**Figure 1.** A schematic of the experimental setup indicating the feed gas tanks, pumps, pressure vessel, nozzle, substrate, and the laser diffraction system.

228

229

## 230 **2.1 Materials**

231 CNCs with an average diameter and length of 3 and 75 nm, respectively were provided by  
 232 CelluForce (Quebec, Canada). CNC with concentration of 0.2, 0.5, 2 wt% were dispersed in 500  
 233 mL of deionized water (DI-H<sub>2</sub>O) using probe sonication (Qsonica Q125 equipped with a 12 mm  
 234 sonotrode) for 30 min at a frequency of 20 kHz and 75% intensity. Sonication was performed at  
 235 room temperature and the colloidal suspension was used within two hours to prevent sedimentation  
 236 and ensure the quality of the dispersion.

237

## 238 **2.2 Test Conditions**

239 **Table 1** represents different test cases and corresponding experimental conditions including  
 240 the concentration of CNC in the injected suspension, injection pressure, and gas-to-liquid ratio  
 241 (GLR). GLR is the ratio of the CO<sub>2</sub> mass flow rate to the liquid (nanoparticle suspension) mass  
 242 flow rate measured upon feeding CO<sub>2</sub> and the liquid separately into the mixing chamber prior to  
 243 injection. GLR is commonly used to represent the gas content in the injection mixture. The axial  
 244 distance from the injection nozzle where droplet Sauter Mean Diameter (SMD) is measured is  
 245 outlined in Table 1. The average size of droplets in a spray is commonly represented by Sauter

246 Mean Diameter (SMD) and is calculated as  $SMD = \frac{D_s^3}{D_v^2}$ , where the surface diameter and volume

247 diameter are defined by  $D_s = \sqrt{\frac{A}{\pi}}$ , and  $D_v = (\frac{6V}{\pi})^{\frac{1}{3}}$ , respectively and  $A$  and  $V$  represent the surface  
 248 area and volume of the droplet, respectively. All experiments were carried out at room conditions  
 249 (25°C and relative humidity ~ 40%).

250

**Table 1.** Design of experiments

CNC Concentration (wt%)	Injection Pressure (MPa)	Axial Distance (cm)	GLR
0.2	3, 6, 7.5, 9	10, 15, 20	0.02, 0.05,
0.5			0.075, 0.1,
2			0.2, 0.5, 1, 2, 3, 4

251

## 252 **2.3 Characterization Techniques**

### 253 **2.3.1 Microscopy**

254 A Leica DM6B (Leica Microsystems Inc., Germany) motorized microscope equipped with 2x-  
 255 40x objectives is used to portray the distribution of droplets on the glass substrate. Polarized light  
 256 mode is applied to visualize the distribution of the crystalline CNCs that are otherwise transparent  
 257 to brightfield lighting.

### 258 **2.3.2 High-Speed Imaging**

259 A Fastcam SA5 (CA, USA) high-speed camera equipped with a Nikon Nikkor (Tokyo, Japan)  
260 micro lens is used for diffuse back-illumination imaging of the spray development. The resolving  
261 power of this optical system correlated with the smallest feature that it can accurately capture is  
262  $\sim 20 \mu\text{m}$ . The images are captured with a frame rate of 500,000 fps and have a  $128 \times 64$  pixels field  
263 of view.

#### 264 *2.3.3 Laser Diffraction*

265 A Malvern Panalytical's laser diffraction system (Malvern, UK) with a He-Ne laser source is  
266 used for real-time measurements of the average volume-based droplet size (SMD) at different axial  
267 locations across the spray. Sampling errors and the back-end algorithms that are deployed in the  
268 system software to convert the scattered light into meaningful particle size measurements are the  
269 main limitations of these systems,<sup>98</sup> yet the system has a 1 Hz acquisition rate,  $0.1 \mu\text{m}$  resolution,  
270 and 99% accuracy in size measurements. Measurements are captured from the diffraction pattern  
271 of the superimposed laser beam and the spray. All reported droplet sizes are at least an average of  
272 six measurement realizations.

#### 273 *2.3.4 Profilometry*

274 Bruker DektakXT Surface Profiler (Bruker Corp., USA.), which is a stylus-based surface  
275 profilometer with a vertical resolution of  $1 \text{ \AA}$ , is used to map the height of CNCs deposited on the  
276 surface of the glass substrates after droplet evaporation. A stylus with a  $6.5 \mu\text{m}$  tip and 3 mg force  
277 is used for all measurements. All experiments were carried out at least six samples and the average  
278 height profile is reported.

#### 279 *2.3.5 Rheometer*

280 A cone-and-plate rheometer (Anton Paar-MCR 301, Austria) is used to measure the viscosity  
281 of aqueous suspensions of CNC with different concentrations at room temperature. All  
282 experiments were repeated at least six times and the average viscosity is reported.

#### 283 *2.3.6 Zetasizer*

284 A Malvern Zetasizer Ultra (Malvern, UK) is used for measuring the diffusion coefficient  
285 of cellulose nanoparticles in water using non-invasive light scattering. All experiments were  
286 repeated at least six times and the average diffusion coefficient for each case is reported.

#### 287 *2.3.7 Post-Processing Methods*

288 ImageJ (NIH) is utilized for post-processing the microscopy images to measure the diameter  
289 of droplets. In order to measure the surface area that is coated with CNC, we have binarized images  
290 by imposing a global intensity threshold above which the intensity was set to one and the remaining  
291 pixel intensities were set to zero. We have then used ImageJ to measure the area covered with  
292 pixels that have the intensity of one. The jet development simulation is visualized using the  
293 EnSight software package from ANSYS. In addition, the Matplotlib library in Python is utilized  
294 to plot and analyze the data from laser diffraction and profilometry techniques.

### 295 **3. Computational Method**

#### 296 *3.1. Governing Equations*

297 Three-dimensional Computational Fluid Dynamics (CFD) simulation is carried out in the  
 298 open-source C++-based CFD package OpenFOAM-2.2.x<sup>99</sup> to model the atomization and breakup  
 299 of the aqueous suspension, formation of the liquid film deposited on the solid substrate, and the  
 300 behavior of the droplets on the substrate that include stick, rebound, spread, and splash.<sup>100</sup> A two-  
 301 dimensional domain is considered for simulating the liquid film on the solid substrate. Dynamic  
 302 structure Large Eddy Simulation (LES) is implemented in this study<sup>101</sup> to incorporate the  
 303 turbulence effect of the fluid phase (liquid suspension and the surrounding gas) and Stanton-  
 304 Rutland model is employed to model film formation on the solid substrate.<sup>102</sup> A Lagrangian-  
 305 Eulerian approach<sup>103</sup> is used for the spray simulation that treats the gas phase as a continuum for  
 306 which a complete set of transport equations are solved while the liquid phase is considered as a  
 307 discrete phase transported with the gas medium. The sub-models used for the spray simulation  
 308 include the dispersion model, Kelvin-Helmholtz Rayleigh-Taylor (KH-RT) breakup model<sup>104</sup>,  
 309 vaporization model<sup>105</sup>, Ranz-Marshall<sup>106</sup> heat transfer model, and dynamic structure turbulence  
 310 model. For the sake of brevity, we only discuss the modified transport equations employed for  
 311 solving the continuity (Eq. 1) and momentum for the liquid film deposited on the substrate (Eq.  
 312 2). For the details on Lagrangian–Eulerian spray simulations, the reader is referred to the authors’  
 313 earlier works.<sup>107, 108</sup> The heat transfer on the solid substrate has been neglected here to isolate the  
 314 behavior of the splashing droplets upon reaching the substrate from evaporation effects. It is noted  
 315 that small droplets may have a non-Newtonian behavior due to the presence of the nanoparticles;  
 316 however, as the CNC concentration is low, this study assumed a Newtonian behavior.

$$\frac{\partial \delta}{\partial t} + \frac{1}{A_{wall}} \sum_{i=1}^{N_{side}} (\vec{V}_{film} \cdot \hat{n})_i \delta_i l_i = \frac{S_d}{\rho_l A_{wall}}, \quad (1)$$

$$\begin{aligned} & \frac{\partial(\delta \cdot \vec{V}_{film})}{\partial t} + \frac{1}{A_{wall}} \sum_{i=1}^{N_{side}} \vec{V}_{film} (\vec{V}_{film} \cdot \hat{n})_i \delta_i l_i \Phi_i \\ & = \frac{-\sum_{i=1}^{N_{side}} (P \hat{n})_i \delta_i l_i}{\rho_l A_{wall}} + \frac{M_{tang}}{\rho_l A_{wall}} + \frac{\sum_{i=1}^{N_{side}} \vec{\tau} A_i}{\rho_l A_{wall}}, \end{aligned} \quad (2)$$

317 The continuity and momentum equations are presented in (1) and (2), respectively and  $A_{wall}$  is the  
 318 area of the wall cell,  $\vec{V}_{film}$  is the film velocity,  $l_i$  is the substrate length at side  $i$ ,  $\rho_l$  is the film  
 319 density,  $\delta_i$  is the film thickness at side  $i$ ,  $\Phi_i$  is the impingement angle, and  $S_d$  is the source term.  
 320 The following equations are used to calculate the pressure as  $P = P_{cell} + P_d$ , where  $P_{cell}$  is the free  
 321 stream pressure.  $P_d$  is the dynamic pressure due to impingement and splashing of the droplets  
 322 defined as follows:

$$P_d = \rho_l \sum_{i=1}^{N_{drop}} V_{nd}^2 \frac{A_{di}}{A_{wall}} + \rho_l \sum_{j=1}^{N_{splash}} V_{nj}^2 \frac{A_j}{A_{wall}}, \quad (3)$$

323 where  $V_{nd}$  is the normal component of velocity of the incoming droplets and  $V_{nj}$  is the normal  
 324 component of velocity of the  $j^{\text{th}}$  secondary droplet due to splashing.  $A_{di}$  and  $A_j$  are projected areas

325 of the  $i^{\text{th}}$  incoming droplet and  $j^{\text{th}}$  splashed droplet, respectively.  $M_{tang}$  is the tangential momentum  
 326 due to the impingement and splashing of the droplets defined as follows:

$$M_{tang} = \sum_{i=1}^{N_{drop}} (m_i \vec{V}_{\tau_{di}}) - \sum_{j=1}^{N_{splash}} (m_j \vec{V}_{\tau_j}). \quad (4)$$

327 Finally, the shear force acting on the substrate due to the droplet splashing is defined as

$$\sum_{j=1}^{N_{edge}} (A_j \vec{\tau}_j) = \sum_{i=1}^{N_{splash}} (\vec{\tau})_{edge,i} \delta_i l_i + (\vec{\tau})_{wall} A_{wall} + (\vec{\tau})_{liq/air} A_{wall}, \quad (5)$$

328 where  $(\vec{\tau})_{edge,i}$  is the shear stress along the edges of the film,  $(\vec{\tau})_{wall}$  is the wall shear stress, and  
 329  $(\vec{\tau})_{liq/air}$  is the shear stress at the interface between the gas and the liquid.

330

### 331 **3.2 Droplet Behaviour on the Substrate**

332 The droplet behavior upon reaching the substrate is detected via the droplet splashing criteria  
 333 suggested by Stanton <sup>109</sup> as outlined in **Table 2**. It indicates whether the droplets stick, rebound,  
 334 or spread on the solid substrate depending on the frequency of the incoming impinging droplets.  
 335 This criterion is based on the Weber number ( $We$ ) that is defined as the ratio of the drag force to  
 336 surface tension force acting on the droplets. The parameters given in **Table 2** include  $d_d$ , the  
 337 diameter of impinging droplet;  $f$ , the frequency of droplets impinging on the wall,  $v$ , the velocity,  
 338 and  $\sigma$  is the surface tension coefficient.

339

**Table 2.** Droplet splashing criteria <sup>109</sup>

Stick	$We < 5$
Rebound	$5 < We < 10$
Spread	$10 < We < 324v^{1/4}f^{3/4}(\rho/\sigma)^{1/2}$
Splash	$We > 324d_d v^{1/4}f^{3/4}(\rho/\sigma)^{1/2}$

340

341 We will calculate the velocity of the droplets after rebound and the angle at which the  
 342 droplets bounce off from the substrate. We will identify the position of the droplets based on their  
 343 velocity upon impact with the substrate to predict the liquid film growth towards the edges of the  
 344 substrate as the droplets stick to the substrate. The number density of the droplets bouncing off the  
 345 substrate will be calculated. Finally, a Weibull distribution <sup>110</sup> is used to calculate the diameter of  
 346 the droplets which break down and bounce back from the surface of the liquid film on the substrate.  
 347 The equations used for calculating the above-mentioned parameters are summarized in *Appendix*  
 348 *I*.

## 349 **4. Results and Discussion**

### 350 **4.1 Spray Formation**

351 It is crucial to understand the breakup mechanisms of the supercritical CO<sub>2</sub>-assisted  
 352 atomization of the aqueous CNC suspension as it creates droplets that carry and deposit the  
 353 nanoparticles on the substrate. In order to fully understand the effect of different parameters on the

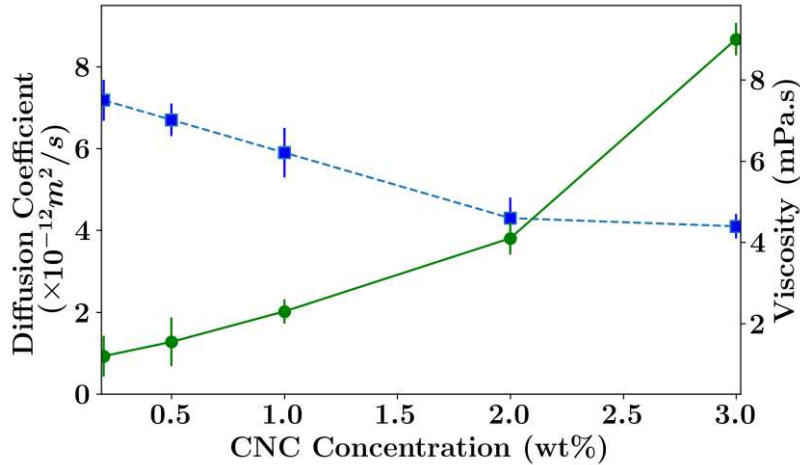
354 deposition process and the created micro/nano structure, a wide range of test cases outlined in  
 355 **Table 1** are studied. The experiments are designed to encompass different phases (i.e., subcritical,  
 356 critical, and supercritical phases) of the hybrid CO<sub>2</sub>-water mixture. Supercritical CO<sub>2</sub> (SC-CO<sub>2</sub>)  
 357 has a high density and is highly soluble in water around the critical point of the CO<sub>2</sub>-water mixture,  
 358 since the diffusion coefficient of CO<sub>2</sub> significantly increases close to this critical pressure (i.e.,  
 359 ~7.5 MPa). The high solubility of CO<sub>2</sub> in water reduces the interfacial tension of the injection  
 360 mixture that is shown to facilitate the atomization process<sup>111, 112</sup>. **Table 3** presents the  
 361 thermophysical properties of CO<sub>2</sub>-water mixture at sub-critical, critical, and supercritical states.  
 362 Comparing these values shows that that optimum condition (high diffusion coefficient and low  
 363 interfacial tension) is achieved at the critical pressure of the CO<sub>2</sub>-water mixture and supercritical  
 364 pressure. Increasing the pressure beyond 9 MPa does not further change the solubility and the  
 365 interfacial tension. The translational diffusion coefficient of CNC in water is measured using  
 366 dynamic light scattering (DLS) and is plotted as a function of CNC concentration in **Fig. 2**. By  
 367 increasing the concentration of CNC from 0.2 to 2wt%, the measured diffusion coefficient  
 368 decreases, and viscosity increases.

369 **Table 3.** Thermophysical properties of subcritical, critical, and supercritical CO<sub>2</sub>-H<sub>2</sub>O.<sup>113, 114</sup>

Pressure (MPa)	CO <sub>2</sub> solubility (mol%)	CO <sub>2</sub> diffusion coefficient (m <sup>2</sup> /s) × 10 <sup>-10</sup>	Interfacial tension (mN/m)	Density (kg/m <sup>3</sup> )
3	1.35	6.7	56.5	1015.2
6	2.15	15.1	40.8	1016.1
7.5	2.35	18.5	36.2	1018.5
9	2.41	13.9	33.5	1020.3

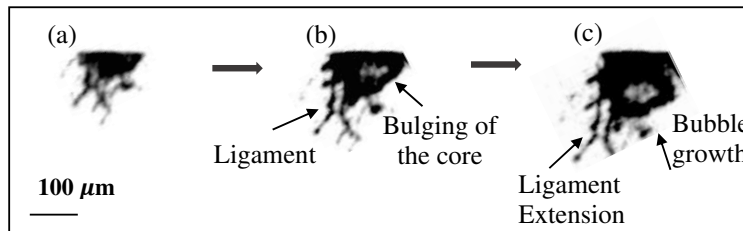
370  
 371 High mole fraction of dissolved SCO<sub>2</sub> in aqueous CNC suspension results in the formation of  
 372 a bulged core filled with CO<sub>2</sub> in the liquid jet very close to the nozzle. The emergence of gas  
 373 bubbles and depressurization into the atmospheric pressure causes bubble expansion and  
 374 eventually bubble burst. The force produced by the bubble burst shatters the liquid into micron-  
 375 size long and slender ligaments that eventually breakup and form small droplets<sup>85</sup>. The temporal  
 376 development of the bubbles and ligaments in a region close to the nozzle (~ 300 μm downstream  
 377 of the orifice exit) is portrayed in **Fig. 3**. The lower interfacial tension of CO<sub>2</sub>-water mixture at  
 378 supercritical conditions facilitates the ligament breakup and the combined effects result in  
 379 enhanced primary breakup and formation of fine droplets with homogenous size distribution that  
 380 ensures a uniform distribution of the deposited nanostructures on the substrate upon evaporation  
 381 of the solvent. We have detailed the breakup mechanism of the liquid jet in the same SAA system  
 382 in our earlier paper<sup>85</sup>.

383



384  
 385 **Figure 2.** Diffusion coefficient of CNC in water (left axis, dashed blue line), and viscosity of aqueous  
 386 CNC suspension (right axis, solid green line) as a function of CNC concentration.  
 387

388 The droplets created through the atomization process carry the nanoparticles and place them  
 389 on the substrate. The assembly of the nanoparticles and the pattern of the deposited nanoparticles  
 390 are highly affected by the droplet evaporation dynamics on the substrate and the size of the  
 391 droplets. As a result, it is important to understand the effect of different spray parameters (i.e.,  
 392 injection pressure, gas-to-liquid ratio, axial distance from injection orifice) and injection mixture  
 393 properties (i.e., the concentration of nanoparticles) on the droplet average size. These analyses will  
 394 aid in designing the process parameters of the spray system. The next section discusses the effect  
 395 of various process parameters on the SMD of the droplets containing nanoparticles.



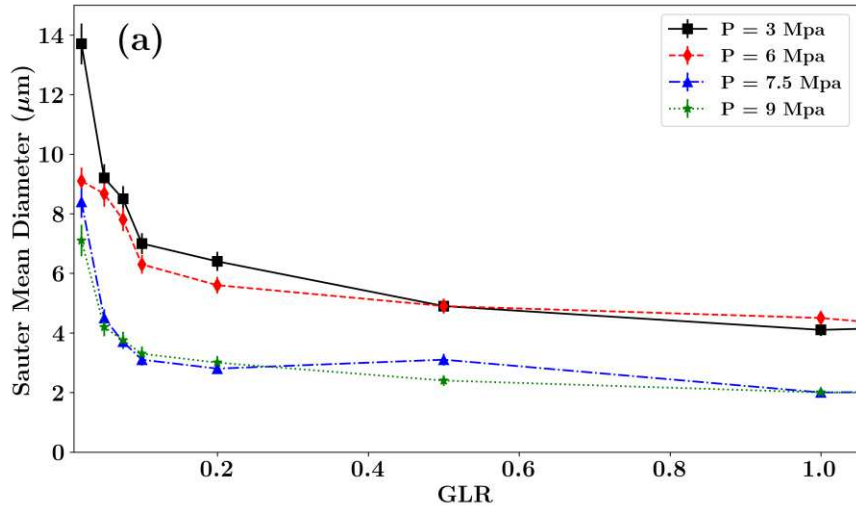
396  
 397 **Figure 3.** High-speed images (500,000 fps) capturing the early development of the spray. GLR = 0.2,  
 398  $P_{inj} = 9$  MPa developing with time from left to right with a  $2 \mu\text{s}$  time interval between the frames.  
 399

#### 400 4.2 Droplet Size Distribution

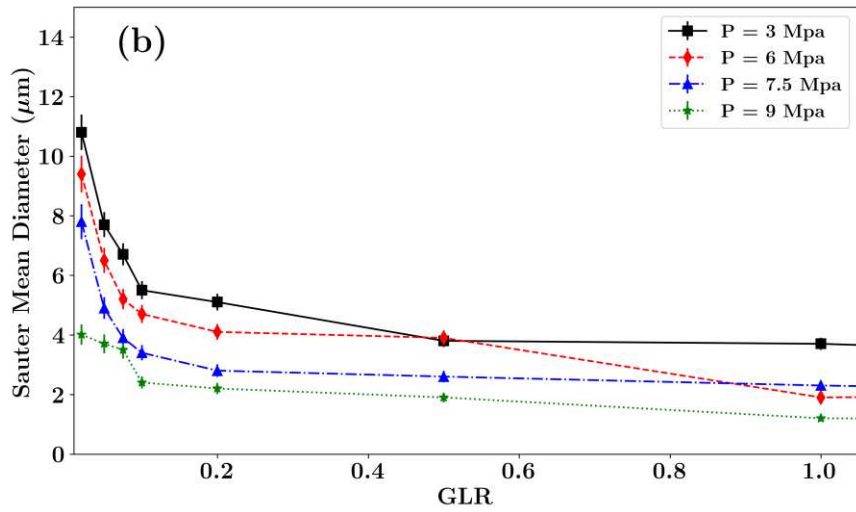
401 The effect of different spray parameters and physical properties of the injection mixture on the  
 402 average size of carrier droplets that is especially crucial for designing the nanoparticle delivery  
 403 system is discussed in this section. The laser diffraction system is used for real-time measurement  
 404 of SMD at 10, 15, and 20 cm axially located downstream of the nozzle. These points are selected  
 405 to fully represent the whole spray plume. **Figure 4** plots the measured SMD as a function of GLR  
 406 for different injection pressures and axial locations. It is observed in **Fig. 4 (a-c)** that for each  
 407 injection pressure, the mean droplet size decreases as GLR increases and the rate of SMD reduction  
 408 decreases with an increase in GLR and reaches a plateau at the GLR of 0.2. At this point, increasing

409 GLR does not have a noticeable effect on the SMD and hence this value (i.e., GLR= 0.2) is selected  
410 for spray deposition experiments.

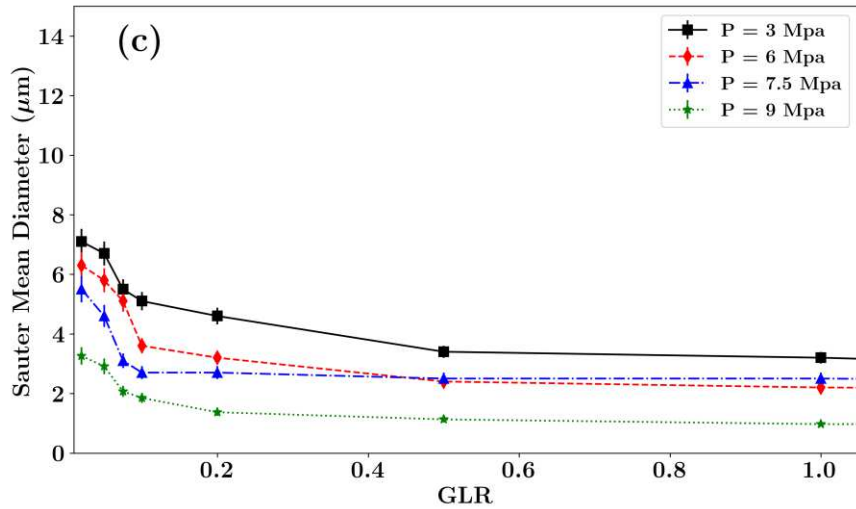
411 At each GLR and axial distance, increasing the injection pressure results in the formation of  
412 droplets with smaller sizes. This is owed to the higher solubility of CO<sub>2</sub> in water and lower  
413 interfacial tension of CO<sub>2</sub>-water mixture at higher pressures as was indicated in **Table. 3**. The  
414 combined effects enhance the primary breakup of the liquid jet due to the burst of dissolved gas  
415 bubbles and surface capillary breakup. As a result, the variation of droplet sizes by changing  
416 injection pressure is more evident in cases where measurement is performed closer to the nozzle  
417 (i.e., 10 cm axial distance in **Fig. 4(a)**) compared to measurements further away from the injection  
418 orifice (i.e., 15 and 20 cm from the orifice in **Fig. 4(b, c)**). It is also evident that for each injection  
419 pressure, increasing the axial distance between the injection orifice and SMD probe from 10 cm  
420 in **Fig. 4a** to 20 cm in **Fig. 4c**, results in smaller mean droplet sizes and their size does not vary  
421 significantly with GLR. This can be attributed to the “secondary breakup” of droplets that occurs  
422 at locations further away from the nozzle. The secondary breakup is referred to a process in which  
423 the droplets exposed to high shear forces breakup into multiple smaller droplets.



424



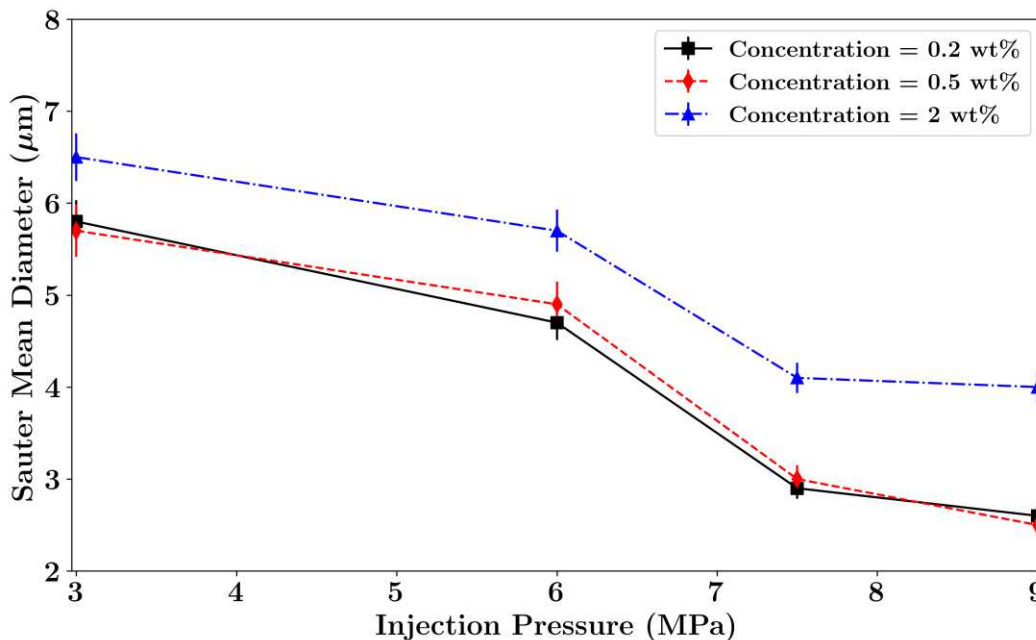
425



426

427 **Figure 4.** SMD measurements as a function of GLR for different injection pressures and an axial distance  
 428 of (a) 10 cm, (b) 15 cm, and (c) 20 cm from injection orifice.

429 **Figure 5(a)** shows the measured SMD as a function of injection pressure at 1 cm axial distance  
 430 with respect to the nozzle and for three different concentrations of CNC in the suspension (i.e.,  
 431 0.2, 0.5, and 2wt%). Similar to **Fig. 4**, increasing the injection pressure reduces the droplet sizes.  
 432 The droplet sizes breakup into smaller droplets at locations further away from the orifice due to  
 433 the secondary breakup. The sharpest decrease in the droplet is achieved at 7.5 MPa injection  
 434 pressure that is close to the critical pressure of the CO<sub>2</sub>-water mixture. The proximity to the critical  
 435 pressure enhances the diffusivity of CO<sub>2</sub> in water and the creation of more bubbles inside water  
 436 upon injection that enhances the atomization process and reduces the droplet size. Further  
 437 increasing the injection pressure to 9 MPa has a negligible effect on the droplet size. This can be  
 438 attributed to the maximum diffusion coefficient of CO<sub>2</sub> in water that occurs at 7.5 MPa,<sup>115</sup> which  
 439 in turn results in minimum surface tension value for the water-CO<sub>2</sub> mixture at this pressure.<sup>114</sup> In  
 440 addition, increasing the concentration of nanoparticles in the injection mixture, from 0.2wt% to  
 441 2wt%, increases the overall size of the carrier droplets. The viscosity of the aqueous suspension  
 442 increases from 1.2 to 4 mPa.s by increasing the concentration from 0.2 to 2wt% as indicated in  
 443 **Fig. 2**. This enhancement (~three-fold) in viscosity of the injection mixture leads to an average of  
 444 ~54% growth in droplet sizes of the spray. It is well established that an increase in liquid viscosity  
 445 results in the formation of larger droplets as it suppresses the breakup process by dampening the  
 446 interfacial perturbations between the liquid and gas upon injection that eventually break it up to  
 447 multiple droplets.<sup>116, 117</sup> The direct effect of droplet sizes on the dynamics of solvent evaporation  
 448 which in turn influences the assembly of nanoparticles and architecture of nanostructures formed  
 449 on the substrate is discussed in the next section.

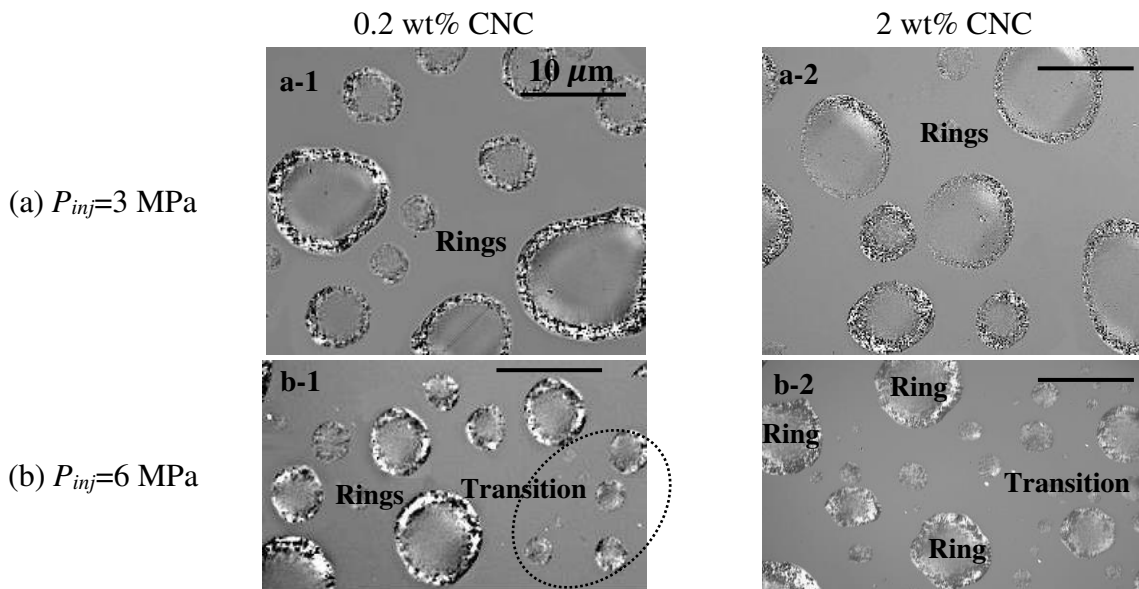


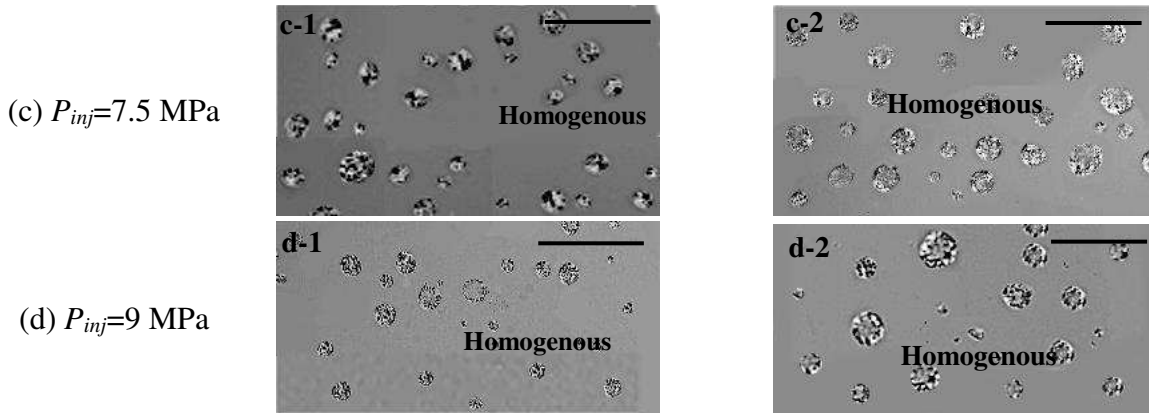
450 **Figure 5.** SMD as a function of injection pressure for different CNC concentrations measured at an axial  
 451 distance of 15cm and GLR=0.2.  
 452  
 453

454 **4.3 Nanostructure Patterns**

455 In this section, we discuss the CNC patterns that form after the evaporation of the liquid  
 456 droplets generated through atomization of the aqueous CNC suspension. We study the effects of  
 457 different process parameters on the created nanostructure on a glass substrate. **Figures 6** visualizes  
 458 the polarized micrographs of otherwise transparent CNC nanostructures that are formed on the  
 459 substrate upon droplet evaporation for different injection pressures. The glass substrates are 1cm  
 460 by 1 cm. **Figure 6** illustrates the architecture of nanostructures for various injection pressures for  
 461 0.2wt% (left column) and 2wt% (right column) CNC concentration. The main pattern of assembled  
 462 nanostructures in these top-view micrographs can be categorized in one of the three shapes: (1)  
 463 ring-shape, where the majority of nanoparticles accumulate along the edge of the evaporating  
 464 droplet, (2) homogenous distribution, where particles scatter across the surface area of the  
 465 evaporating droplet, and (3) transition stage, where there is still a distinct ring-shape structure and  
 466 some particles are also scattered within the center of the evaporating droplet. It is illustrated in **Fig.**  
 467 **6(a1-d1)** that regardless of the injection pressure, the droplets with diameters smaller than  $\sim 5.5 \mu\text{m}$   
 468 exhibit a homogenous distribution, while droplets larger than  $\sim 7.5 \mu\text{m}$  have generated a ring-  
 469 shaped structure, and droplets with diameter sizes in between the two thresholds (i.e., between 5.5  
 470 to  $7.5 \mu\text{m}$ ) represent a transition between the two identified regimes. All three patterns were  
 471 observed for all injection pressures as the droplet size distribution envelopes the detected  
 472 thresholds. In **Fig. 6(a2-d2)** that illustrate droplets with a higher concentration of CNC particles  
 473 (i.e., 2wt%), the homogenous distribution, transition, and ring structure occurs for  $< 9.5 \mu\text{m}$ ,  $\sim 9.5$ -  
 474  $11.5 \mu\text{m}$ , and  $> 11.5 \mu\text{m}$  droplet sizes, respectively. It is noted that at least 6 images were taken at  
 475 different locations of the same substrate; all of which were in great agreement with the threshold  
 476 detected in these figures.

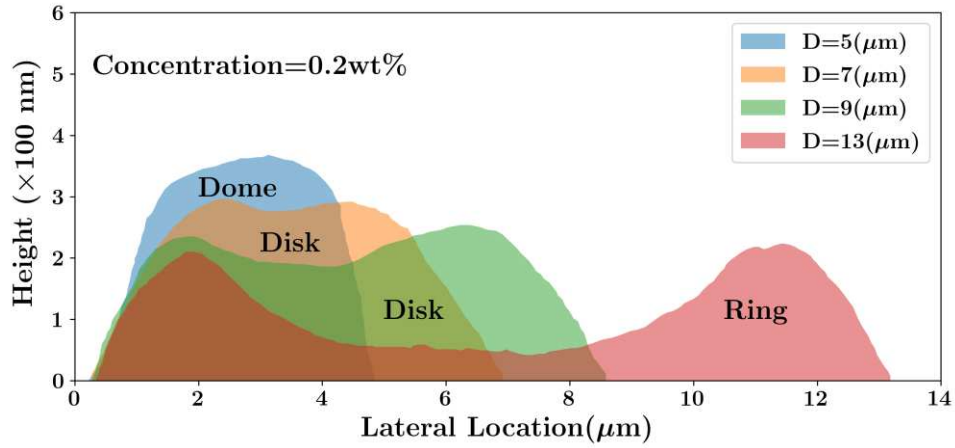
477



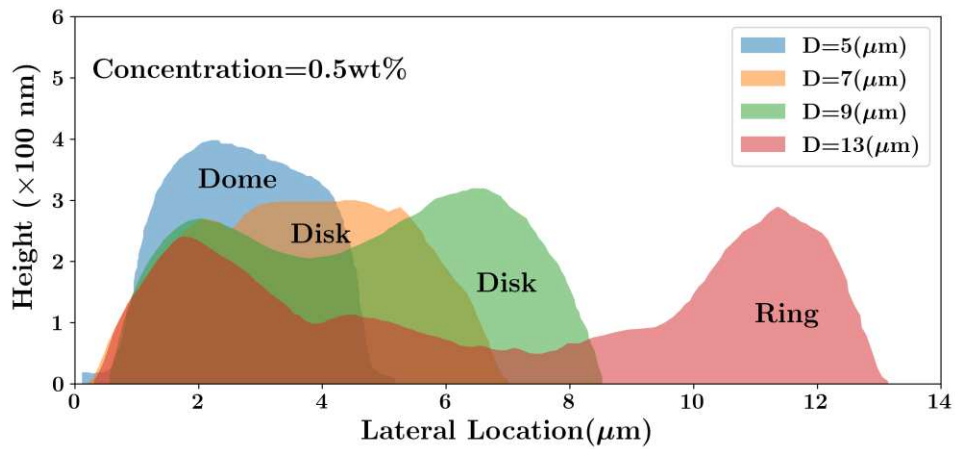


478 **Figure 6.** Polarized microscopy of CNC patterns after evaporation of water in CNC aqueous suspension  
 479 droplets on a glass substrate located at 15cm axial distance for 0.2 wt% CNC concentration for (a-1) 3  
 480 MPa, (b-1) 6 MPa, (c-1) 7.5 MPa, and (d-1) 9 MPa injection pressures and 2 wt% CNC concentration for  
 481 (a-2) 3 MPa, (b-2) 6 MPa, (c-2) 7.5 MPa, and (d-2) 9 MPa injection pressures. The 10  $\mu\text{m}$  scale bar is  
 482 identical in all images.  
 483

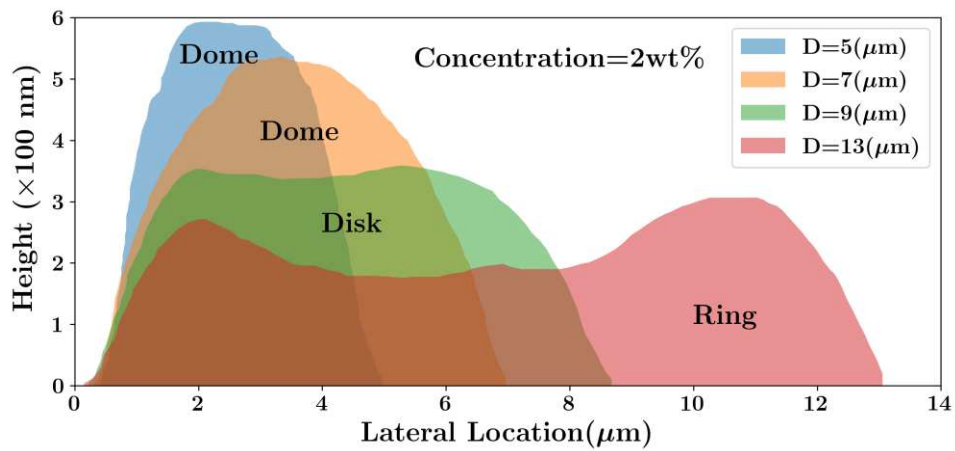
484 **Figure 7** demonstrates the profile/height measurements of assembled nanostructures upon  
 485 evaporation for droplet sizes varying from 5 to 13  $\mu\text{m}$  and different concentrations (0.2wt%,  
 486 0.5wt%, 2wt%). Combined with top-view micrographs presented in **Fig. 6**, they provide a 3D  
 487 realization of the shape of assembled CNC nanostructures. In **Fig. 7**, the droplets have been  
 488 injected at 9 MPa. We discussed the effect of injection pressure on the nanoparticle patterns in **Fig.**  
 489 **6** and showed that droplets with the same size and concentration shared the same pattern regardless  
 490 of the injection pressure. The profilometry height measurements indicate that nanostructures  
 491 represent a ring, disk, or dome shape. A ring pattern that is identified with two peaks on the height  
 492 profile is referred to the accumulation of nanoparticles along the edge of the droplet (labeled as  
 493 “ring” in the top view in **Fig. 6**). A dome forms when nanoparticles are captured at the interface  
 494 during evaporation and mainly remained in the center after droplet evaporation i.e., only one peak  
 495 is observed on the height profile. The dome structure was identified as “transition” in the top view  
 496 depicted in **Figure 6**. Finally, a disk pattern forms when the height profile is nearly flat at the  
 497 center. This indicates nanoparticles are scattered more uniformly across the surface area of the  
 498 droplet compared to the dome and ring and. The disk pattern was identified as “homogenous” in  
 499 the top view **Fig. 6**. **Figure 7** shows that by decreasing the droplet size from 13  $\mu\text{m}$  (red) down to  
 500 5  $\mu\text{m}$  (blue), the assembly of particles transits from ring-shape to a dome-shape structure for all  
 501 CNC concentrations. The 9  $\mu\text{m}$ -droplet (green) represents the transition between ring to a disk-  
 502 shape structure. By increasing the concentration of CNC, the transition from a ring structure to  
 503 disk occurs at larger droplet sizes. As will be discussed in the next section, the droplet size and  
 504 concentration directly affects the evaporation rate of the solvent, which in turn influences the  
 505 particle advection and diffusion and ultimately the nanoparticle patterns.



506



507



508

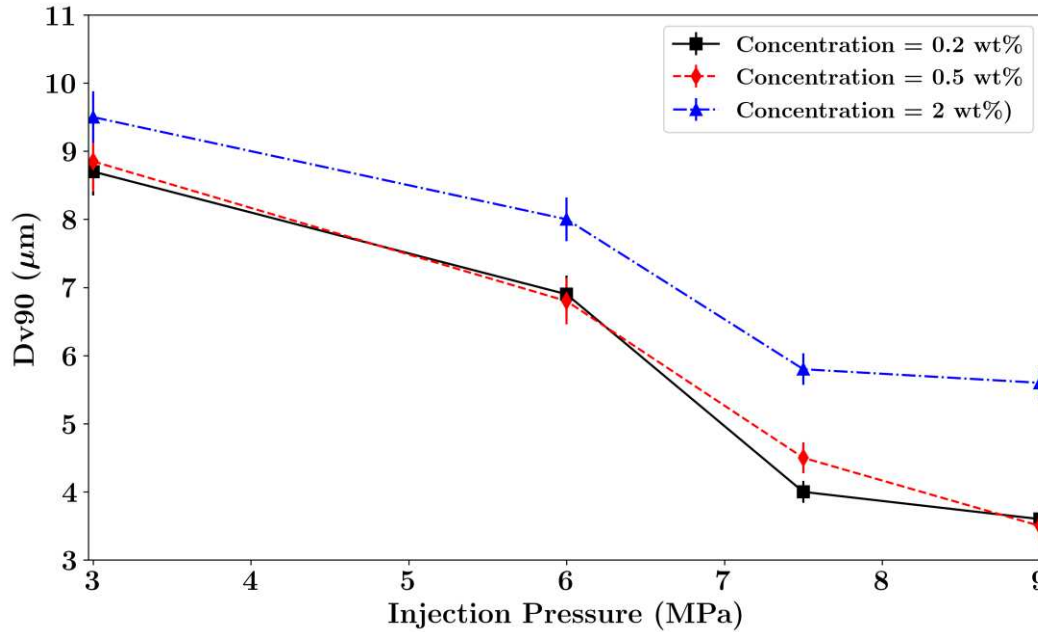
509

510

511

512

**Figure 7.** Profilometer height measurement of CNC nanostructures created on substrate after evaporation of water in droplets as a function of droplet diameter. CNC concentrations are 0.2, 0.5, and 2wt% and the injection pressure is 9 MPa.



513 **Figure 8.** Dv90 as a function of injection pressure for different CNC concentrations measured at an  
 514 axial distance of 15cm and GLR= 0.2.  
 515

516 In summary, by controlling the droplet sizes we can engineer the desired pattern (ring, dome,  
 517 disk) for different concentrations. The use of SCO<sub>2</sub> enables achieving a very uniform distribution  
 518 of droplet sizes within the spray that facilitates achieving a uniform distribution of CNC with the  
 519 desired pattern on the substrate. The injection pressure can directly control the overall size of  
 520 droplets within the spray plume and can be adjusted to the size requirements of the specific  
 521 application where the spray deposition system is being used. To quantitatively demonstrate the  
 522 control over the nanostructure patterns with the injection pressure Dv90 measurement using laser  
 523 diffraction method is plotted vs. injection pressure for variable concentrations plotted in **Fig. 8**.  
 524 Dv90 indicates the mean diameter size that represents 90% of the total volume of the existing  
 525 liquid droplets **Fig. 8** shows that at 7.5 MPa injection pressure and 0.2wt% CNC concentration,  
 526 90% of droplets are smaller than 4 μm in size. Based on the microscopic images and height  
 527 profilometry, droplet sizes smaller than 4 μm will represent a homogenous nanoparticle  
 528 distribution. As a result, most of the deposited nanostructures will exhibit a disk-shape structure.  
 529 The information from this measurement combined with detailed discussions on the 3D architecture  
 530 of fabricated micro/nanostructures have important implications in designing practical deposition  
 531 systems to ensure that majority (> 90%) of droplets fall under a certain category (i.e., ring versus  
 532 homogenous distribution).

#### 533 4.4. Evaporation-Induced Nanoparticle Assembly

534 In this section, we will explore the CNC assembly in micron-size evaporating droplets.<sup>118</sup>  
 535 <sup>119</sup> In order to find the link between the dynamics of droplet evaporation and the formation of a  
 536 specific pattern upon evaporation, two main parameters are identified: (1) droplet evaporation rate  
 537 that is linked to the convective transport of CNC as the droplet edge recedes back during droplet  
 538 evaporation; and (2) the Brownian diffusion rate of CNC in water. It has been shown that in the

539 absence of other competing mechanisms e.g., external forces, special treatment of the substrate or  
 540 solvent, the competition between the convective and diffusive transport of particles dictates the  
 541 final pattern after droplet evaporation.<sup>120</sup> The ratio of the convective to diffusive transport of  
 542 particles during water evaporation is represented by the non-dimensional Péclet ( $Pe = r^2/Dt_e$ )  
 543 number, where ‘ $r$ ’ is the droplet radius, ‘ $D$ ’ is the particle mass diffusivity in the liquid phase and  
 544 ‘ $t_e$ ’ is the droplet evaporation time. For millimeter-sized droplets, it has been shown<sup>121</sup> that the  
 545 ring pattern is typically favored for  $Pe > 1$  as the convective rate surpasses the diffusive rate. A  
 546 reduction in the  $Pe$ , which implies a diffusion-dominated transport, is known to mitigate the ring  
 547 formation toward a more uniform particle distribution.<sup>122</sup>

548 Our SMD measurements of the spray suggest that the droplet sizes are below 20 microns for  
 549 which measuring the droplet evaporation rate is experimentally very challenging. As an alternative  
 550 approach, there are various mathematical and analytical models to calculate the evaporation rate  
 551 of a sessile droplet.<sup>123-125</sup> Larson’s model (**Eq. 6**), which is applicable for semispherical sessile  
 552 droplets, is commonly used as one of the most accurate models that has been verified empirically.  
 553<sup>123</sup> This model is more accurate when the Bond number is smaller than 0.1 ( $Bo = \frac{\rho g R h_0}{\sigma}$ ) and the  
 554 capillary number ( $Ca = \frac{\mu u_r}{\sigma}$ ) is smaller than 1.  $Bo$  is the ratio of the gravitational to surface tension  
 555 forces and accounts for the initial shape of the droplet whereas  $Ca$  is the ratio of viscous to capillary  
 556 forces and accounts for deformation of the droplet during evaporation. Here  $\rho$ ,  $g$ ,  $R$ ,  $h_0$ ,  $\sigma$ ,  $\mu$ , and  
 557  $u_r$  are the density, gravitational acceleration, contact line radius, initial droplet height, liquid-air  
 558 surface tension, liquid viscosity, and average radial velocity due to evaporation, respectively. We  
 559 first compare the experimentally measured evaporation rate for a 1  $\mu$ l droplet ( $\sim 1$  mm in radius)  
 560 deposited on a glass substrate with the predictions of the Larson’s model. The evaporation rate has  
 561 been measured with a timer at room condition (i.e., 25°C temperature and  $\sim 40\%$  relative humidity).  
 562 Comparing the  $Bo$  ( $\sim 0.07$ ) and  $Ca$  ( $O(10^{-8})$ ) for the largest droplet (i.e., 1mm radius) indicates that  
 563 the droplet has a spherical cap shape and satisfies the requirement for using the Larson’s model  
 564 (**Eq. 6**):

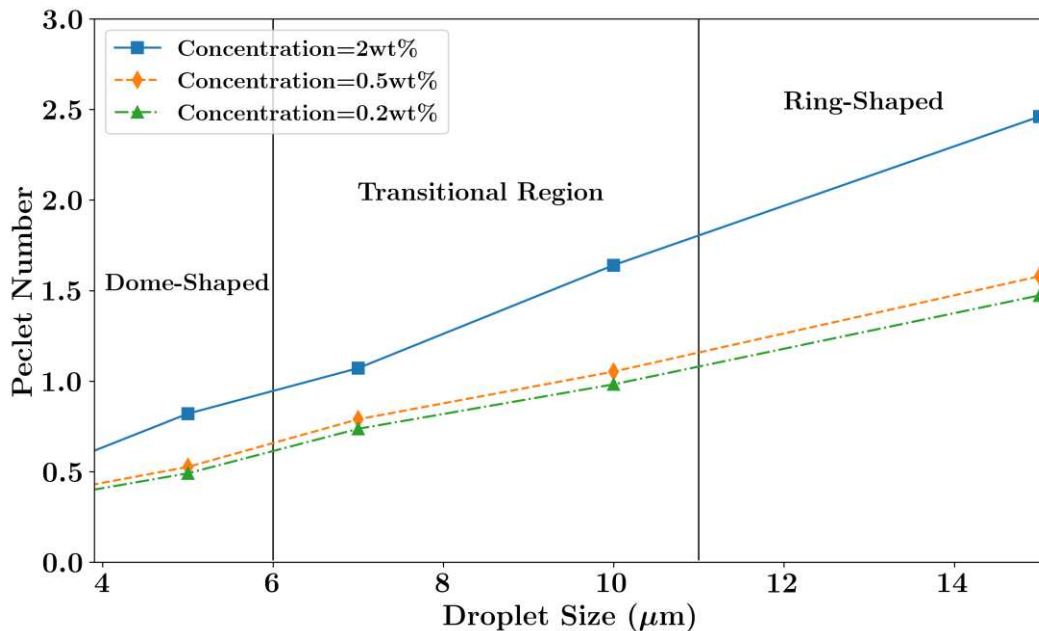
$$\dot{m}(t) = -\pi R D (1 - H) C_v (0.27\theta + 1.3), \quad (6)$$

565 where  $R$ ,  $D$ ,  $H$ ,  $C_v$ , and  $\theta$  are the droplet radius (1mm), water vapor diffusivity ( $2.42 \times 10^{-5} \frac{m^2}{s}$ ),  
 566 relative humidity (40%), saturated water vapor concentration<sup>126</sup> ( $23.2 \frac{g}{mm^3}$ ), and droplet contact  
 567 angle (0.369 rad), respectively. The contact angle is measured on an image that is taken normal to  
 568 a back-illuminated droplet deposited on a solid substrate. Larson’s model predicts 709 seconds for  
 569 a 1 mm droplet to evaporate and our experimental measurement indicated 718 seconds, which is  
 570 in close agreement with the model prediction. The translational diffusion coefficient of CNC in  
 571 DI-water measured by DLS for 0.2, 0.5, and 2wt% concentration (**Fig. 2**) is  $7.18 \times 10^{-12}$ ,  $6.7 \times 10^{-12}$ ,  
 572 and  $4.3 \times 10^{-12} \text{ m}^2/\text{s}$ , respectively. The diffusion coefficient reduces with concentration due to the  
 573 packed space hindering the freedom of particles to transport.<sup>127</sup> We use this data along with the  
 574 evaporation rate obtained from Larson’s model and droplet sizes captured by the laser diffraction  
 575 measurements to calculate  $Pe$ .

576 **Figure 9** shows the calculated  $Pe$  as a function of droplet size for different CNC  
 577 concentrations. By increasing the droplet size for each concentration, the evaporation time is also  
 578 increased while the diffusion coefficient is constant for the same concentration. This results in  
 579 higher  $Pe$  at higher concentrations. According to **Fig. 9**, the corresponding  $Pe$  for a droplet size of  
 580  $13\ \mu\text{m}$  is 1.27, 1.37, and 2.13, for 0.2, 0.5, and 2.0 wt% concentration, respectively.  $Pe > 1$  indicates  
 581 the domination of the convective transport of CNC particles towards the edge of the droplet  
 582 induced by the evaporation of DI-water and formation of a ring-shape structure as was depicted in  
 583 **Fig. 7**. Droplets within the 6-8  $\mu\text{m}$  diameter range have an average  $Pe$  of 0.7, 0.8, and 1 for 0.2,  
 584 0.5, and 2.0 wt% concentration, respectively. These cases where convective and diffusion rates are  
 585 almost equal were identified as the transition between ring and dome shape structures in **Fig. 6**.

586 It is noted that pure CNC is almost hydrophilic, and thus tends to form a ring. However,  
 587 various observed patterns for different concentrations and different droplet sizes imply that in  
 588 addition to the particle shape, level of hydrophilicity, the droplet size, and particle mass  
 589 concentration also play a role in determining the final pattern. For instance, **Fig. 7** showed that for  
 590 a  $9\ \mu\text{m}$ -droplet, the pattern changed from a ring at 0.2 and 0.5wt% to a disk at 2wt%. Our results  
 591 showed that increasing the ratio of mass concentration to droplet size tends to change the pattern  
 592 from ring to dome as the particles are captured at the interface between the evaporating liquid and  
 593 the surrounding air before they get a chance to accumulate at the droplet periphery and dry as a  
 594 dome or disk after liquid evaporation.

595



596

597

**Figure 9.** Peclet number as a function of droplet sizes for different CNC concentrations.

598

#### 599 *4.5 Evaluating the Effectiveness of the Nanoparticle Spray Deposition Method*

600

601

Droplets created by injecting a high-pressure liquid jet toward a substrate in ambient temperature and pressure can evaporate before reaching the substrate, deposit on the substrate, or

602 bounce back from the substrate before depositing their nanoparticle content on the substrate.  
603 Optimizing the distance between the injection orifice and the substrate at different injection  
604 conditions is necessary from two perspectives: (1) to predict and control the evaporation of the  
605 droplets to ensure most of the droplets containing nanoparticles reach the substrate before  
606 evaporation. This is important because if most of the droplets evaporate before reaching the  
607 substrate the nanoparticle content will be dispersed in the surrounding air and wasted; (2) to predict  
608 and control the splashing of the droplets that will affect the nanoparticle content and patterns left  
609 on the substrate. **Figure 11** depicts a series of simulations performed to study the behavior of the  
610 spray and the resulting droplets deposited on the substrate. The black color represents the water,  
611 and the gray shows the ambient air. The droplets are observed around the core of the liquid jet due  
612 to the progression of the atomization process. The distance between the nozzle and the substrate  
613 varies from 5 to 30 cm with 5 cm increments and the tested injection pressure is 3, 6, 7.5, and 9  
614 MPa, consistent with the experiments. The nozzle geometry selected for the simulations is  
615 consistent with the experiment (diameter of 125  $\mu\text{m}$  and cone-angle of  $6^\circ$ ). For the sake of  
616 consistency, a baseline liquid film thickness of 1  $\mu\text{m}$  is set and when this thickness is achieved at  
617 any point on the substrate, it is assumed that the spray has reached the substrate. The simulations  
618 are conducted using pure water at room temperature without considering nanoparticles. Since the  
619 concentration of nanoparticles in water is very low in experiments the nanoparticles do not  
620 interfere with the spray behavior.

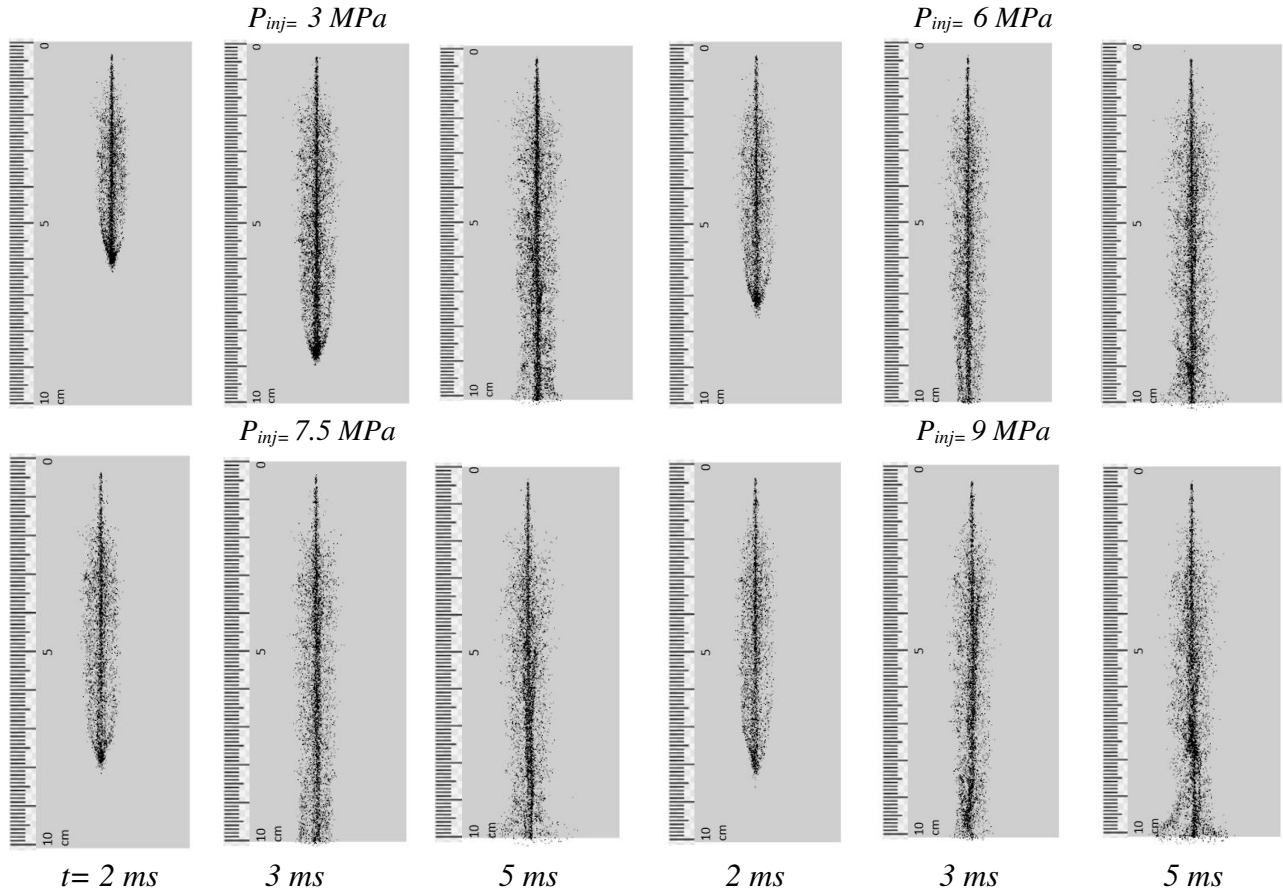
621 The spray development is visualized in **Fig. 10** for the cases where the substrate is located at  
622 10 cm axial distance from the nozzle and injection pressures are 3, 6, 7.5 and, 9 MPa. As **Fig. 10**  
623 shows, increasing the injection pressure and increasing the jet momentum results in longer liquid  
624 penetration length, and thus the time taken to reach the substrate and forming the liquid film  
625 decreases from 4.8 to 2.8 ms by increasing the injection pressure from 3 to 9 MPa. The time  
626 required for the spray to reach the substrate is an important factor in designing experiments and  
627 setting up the optimum location of the substrate. Repeating the simulations for the cases that the  
628 substrate was located at 15 and 20 cm with the same injection pressures of **Fig. 10** revealed that at  
629 20 cm, less than 1% of the droplets reached the substrate which did not result in formation of a  
630 film with 1  $\mu\text{m}$  thickness. These simulations suggest that the substrate should be placed at an axial  
631 distance less than 20 cm from the nozzle to ensure a liquid film of 1  $\mu\text{m}$  thickness is formed on  
632 the nozzle between 3 ms (for 6, 7.5, and 9 MPa) to 4 ms (for 3 MPa) after the start of injection.  
633 Microscopy images of the assembled CNC structures left on the substrate located at 15 cm are  
634 presented in **Fig. 6**.

635

636

637

638

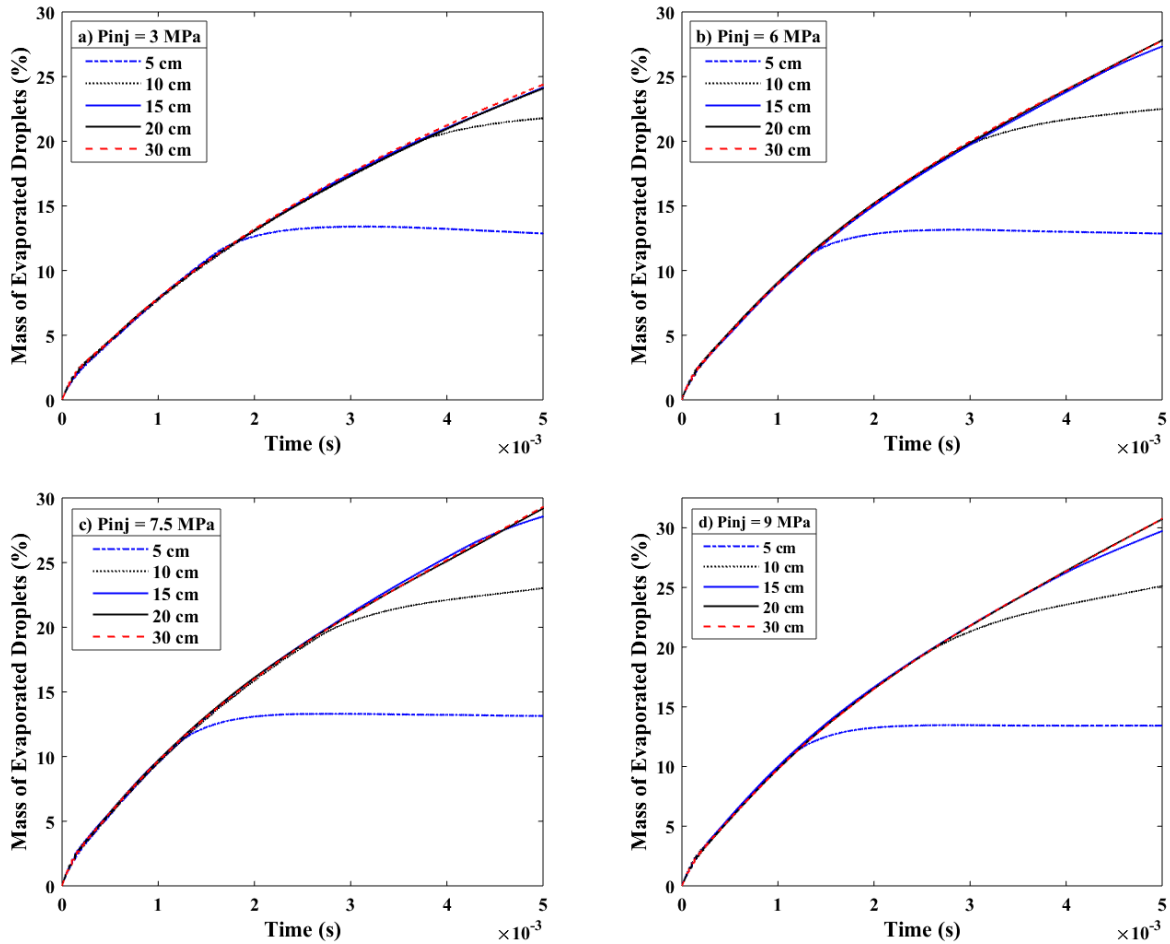


639  
640  
641  
642  
643

**Figure 10.** Computational simulation of spatio-temporal evolution of the spray with different injection pressures at 10 cm distance from nozzle. The black color represents the injected water and gray background represents the surrounding ambient air. The scale bar is identical in all images.

644  
645  
646  
647  
648  
649  
650  
651  
652  
653  
654

Since droplet evaporation before the spray reaches the substrate is essential in efficiently delivering the nanomaterial to the substrate it is imperative to calculate the mass of evaporated droplet as a percentage of the total injected mass as shown in **Fig. 11** for different injection pressures and nozzle-substrate distance. For each injection pressure, increasing the distance between the nozzle and the substrate increases the evaporated mass. The plots reach a plateau once the spray reaches the substrate indicating a relatively constant rates of evaporation. It is seen that for 5 and 10 cm positions, the mass loss due to evaporation of the droplets is in the range of 10-15% and 20-25%, respectively. However, the mass loss reaches 25-30% range for 15 and 20 cm from the nozzle. These observations suggest that placing the substrate at a distance lower than 20 cm below the injection orifice minimizes the mass loss due to evaporation for the explored pressure range of 3 to 9 MPa.



655

656

657

658

**Figure 11.** Temporal variation of the percentage of the mass of evaporated droplets with changes in the distance from the nozzle to the substrate at different injection pressures.

659

660

661

662

663

664

665

666

667

668

669

670

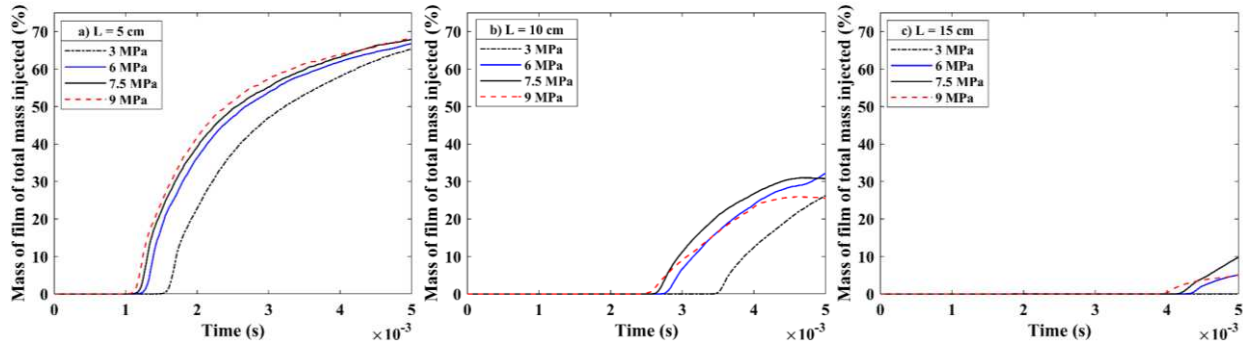
671

672

673

**Figure 12** shows the variation in the percentage of the water mass deposited on the substrate for different injection pressures for substrate positioned at 5, 10, and 15 cm from the orifice. The mass of water deposited on a substrate located 5 cm below the injection point is ~ 65% of the total initial mass upon injection, whereas for a 10 cm distance, 25-30% of its initial mass is deposited. This suggests that the remaining droplets either evaporated or scattered in the surrounding air without reaching the substrate. For 20 and 30 cm nozzle-substrate distance not shown in **Fig. 12**, the simulations predict negligible droplet deposition on the substrate implying that most of the droplets have evaporated before reaching the substrate. At each axial location, increasing the injection pressure results in the delivery of higher portions of the initial mass of droplets to the substrate. However, there is a slight decrease in the deposited mass at 9 MPa injection pressure for the 10 and 15 cm cases. This is because 9 MPa injection pressure generates smaller droplets (as is shown in **Fig. 4** and **5**) which are more prone to evaporation before reaching the substrate. These results suggest that 6 and 7 MPa injection pressures are more appropriate for optimum spray deposition as droplets have large enough momentum to reach the substrate yet the mass of evaporated droplets is smaller than the 9 MPa case before reaching the target substrate. Satisfying

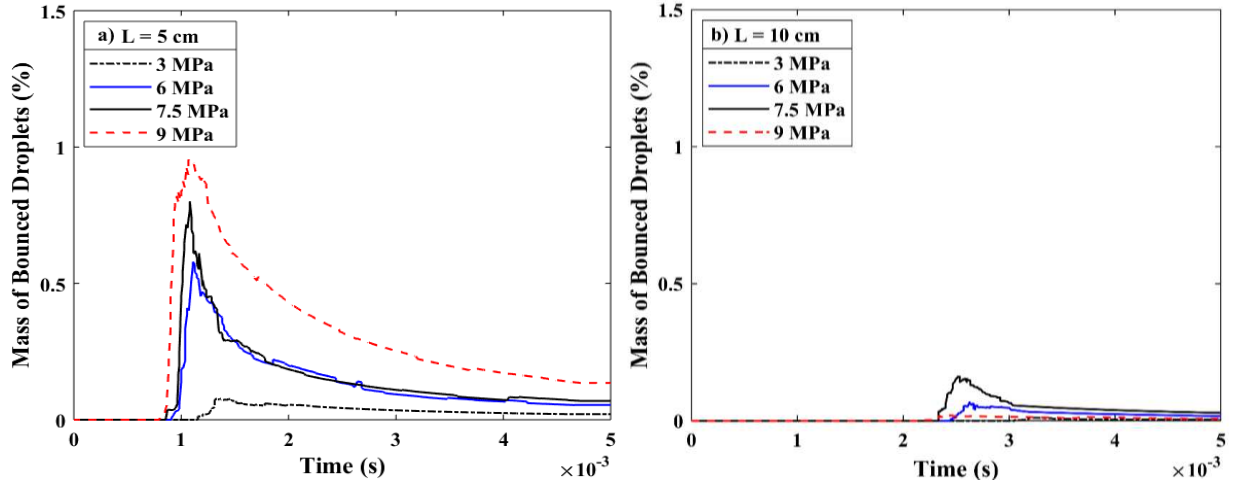
674 these two conditions ensures more efficient delivery of the nanoparticles. In addition, comparing  
675 the experimental measurements of SMD at 7.5 MPa (Figs. 4 and 5) demonstrated a more uniform  
676 and smaller droplet size distribution.  
677



678  
679 **Figure 12.** Temporal variations of the mass of water added to the substrate with the change in injection  
680 pressures for 5, 10 and 15 cm distance between the nozzle and the substrate.

681 The droplet bounce-back upon contact with the substrate is another important factor that affects  
682 the effectiveness of the nanoparticle deposition on the substrate. **Figure 13** represents the water  
683 loss due to splashing from the substrate for axial distances of 5 and 10 cm. As expected, the  
684 percentage of the liquid mass bounced back into the surroundings (~ 0.5-1%) is higher at 5 cm  
685 where the droplets have a higher momentum upon interacting with the substrate. The mass of  
686 bounced droplets at 15 and 20 cm distance are negligible, hence not depicted here. Increasing the  
687 injection pressure to 9 MPa results in higher splashing at the film interface as the droplets gain a  
688 higher momentum upon injection. While positioning the substrate closer to the nozzle may not  
689 seem ideal for a stable film formation due to increased splashing, the percentage of droplets that  
690 are lost due to the bounce-back effect is much lower than the evaporation mass loss (1% versus  
691 20%).

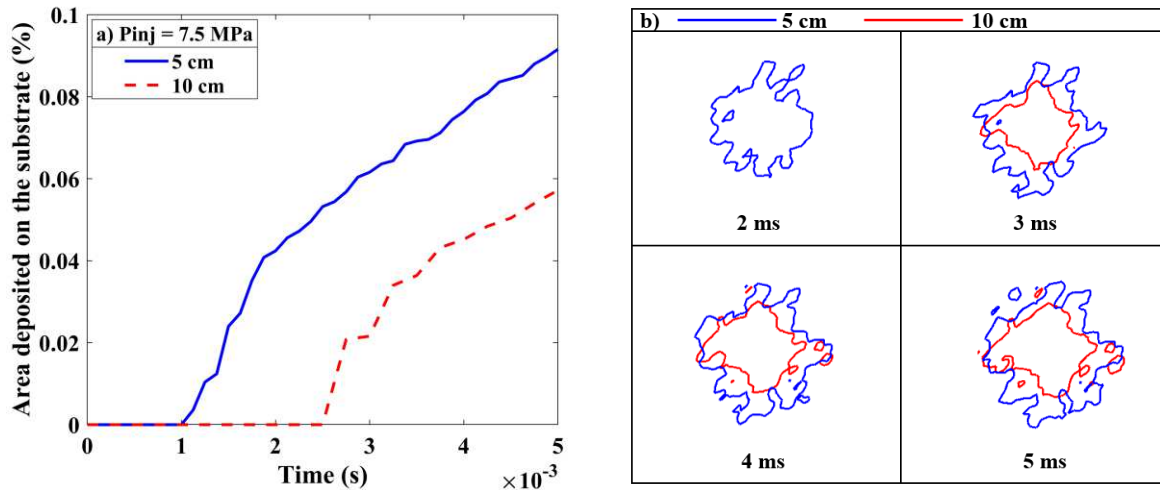
692 Moreover, the higher number of bounced droplets will lead to higher film spread. This happens  
693 when the droplets that have already bounced from the substrate lose momentum and fall back on  
694 the substrate. The temporal variation of the surface coverage and iso-scales of the covered area by  
695 the spray are depicted **Fig. 14**. The film area calculated for 5 cm distance between the nozzle and  
696 substrate (colored with a film thickness of 0.01  $\mu\text{m}$ ) is larger due to enhanced splashing and  
697 subsequent deposition. This eventually leads to higher deposition of nanoparticles and a larger film  
698 front where the nanoparticles accumulate. It can also be seen that there is no deposition for 10 cm  
699 case at 2 ms due to larger distance between nozzle and substrate as compared to the 5 cm case.  
700 Considering different behaviors of droplets (evaporation, deposition, bounce-back) relative to the  
701 axial distance of the substrate observed from simulations, it is concluded that a location between  
702 10-15 cm below the nozzle and 7.5 MPa injection pressure results in a more effective and uniform  
703 nanoparticle deposition



704  
705

706 **Figure 13.** Temporal variations of the percentage of the mass of bounced droplets from the substrate with  
707 injection pressure for 5 and 10 cm distance between the nozzle and the substrate.

708



709

710 **Figure 14.** Temporal variation of the surface covered on the substrate by the film formed due to droplet  
711 deposition for 5 and 10 cm distance between the nozzle and the substrate at 7.5 MPa injection pressure:  
712 (a) percentage of the substrate surface covered, (b) iso-scales depicting droplet deposition of over 0.01  
713  $\mu\text{m}$  film thickness

714

## 715 **Summary and Conclusions**

716 In this study, we designed and built a novel nanoparticle spray deposition system that  
717 utilizes supercritical  $\text{CO}_2$  to assist the atomization process and create uniform micron-size CNC-  
718 carrier aqueous droplets and deposit them onto the substrate to form tailored nanostructures upon  
719 evaporation of water. The effect of spray parameters on formation of droplets were studied  
720 numerically and experimentally. The main conclusions from this work can be summarized as  
721 follows:

722  
723  
724  
725  
726  
727  
728  
729  
730  
731  
732  
733  
734  
735  
736  
737  
738  
739  
740  
741  
742  
743  
744  
745  
746  
747  
748  
749  
750  
751  
752  
753  
754  
755  
756  
757  
758  
759  
760  
761

1. Supercritical CO<sub>2</sub>-assisted atomization sparks two concurrent mechanisms to boost liquid atomization: reducing the liquid surface tension and enhancing CO<sub>2</sub> dissolution in water. The combined effect results in the formation of fine droplets with a narrow size distribution that can be used as nanoparticle-carrier droplets.
2. Laser diffraction measurement of SMD shows that in general, increasing the injection pressure, GLR, and axial distance from the injection orifice results in the creation of smaller droplets. In addition, increasing the concentration of CNC in the injection mixture increases the overall size of the carrier droplets.
3. However, increasing the injection pressure above the critical pressure of the CO<sub>2</sub>-water mixture (i.e., 7.5 MPa) and increasing the GLR do not noticeably decrease the droplet sizes. This means there is no need for extremely high pressures or excessive amount of assisting gas to create micron-sized droplets.
4. Microscopic visualization of the assembled nanoparticles on the substrates illustrates that morphology of nanostructures falls into three main categories: (1) ring-shape pattern, where the majority of nanoparticles accumulate along the edge of the evaporating droplet, (2) homogenous distribution or disk pattern, where particles scatter more uniformly across the surface area of the evaporating droplet, and (3) transition stage, where there is still a distinct ring-shape structure yet some particles are scattered within the edges of the evaporating droplet.
5. The profilometry height measurements combined with micrographs provide a 3D visualization of the assembled nanostructure and show that they either form a ring, disk, or dome-shaped architecture. Increasing the mass concentration to droplet size ratio shifts the morphology of assembled nanoparticles from ring to dome as the particles are trapped at the liquid-air interface before they get a chance to move towards the edge of the droplet.
6. For each CNC concentration and regardless of the injection pressure, there is a droplet size threshold range above which the assembled nanostructures exhibit a ring pattern and below that they exhibit a homogenous distribution. For concentration of 0.2wt%, the lower and upper bounds of the threshold are 5.5 and 7.5  $\mu\text{m}$ , respectively while for 2wt% CNC concentration these values increase to 9.5  $\mu\text{m}$  and 11.5  $\mu\text{m}$ , respectively.
7. The injection pressure on the other hand dictates the size of the majority of droplets within the spray plume and can be used to design a system where the bulk of droplets fall under one of the identified nanostructure patterns.
8. The size of the carrier droplets strictly influences the evaporation rate of solvent in particle-carrier droplets upon deposition on the substrate. The evaporation rate in turn, affects the prevalence of convective to diffusive transport of particles that is represented by Peclet number.
9. The evaporation time is prolonged by increasing the droplet size for each concentration, which results in  $Pe > 1$  that indicates the higher rate of convective transport of particles to diffusive transport leading to accumulation of particles along the periphery of the droplet

762 and formation of a ring-shaped structure. At  $Pe < 1$  where the diffusive movement of CNCs  
763 is dominant, a dome-shaped structure is formed for all tested concentrations. At  $Pe \sim 1$ ,  
764 droplets fall in the transitional region where both ring and dome-shaped structures are  
765 observed.

766 10. Computational simulations show that considering different droplet behavior interacting  
767 with the substrate (evaporation, deposition, bounce-back) versus the injection pressure and  
768 axial distance between the substrate and nozzle, positioning the substrate at 10 or 15 cm  
769 below the nozzle and 7.5 MPa injection pressure result in a more effective and uniform  
770 nanoparticle deposition.

771

## 772 **Declarations**

773

774 Availability of data and materials: All the data and materials supporting the claims herein are  
775 included in the manuscript and comply with the field standards.

776

777 Conflict of interest: The authors declare no conflict of interest

778

779 Funding sources: Not applicable

780

781 Code Availability: Not applicable

782

783 **Appendix I**

784

785 Splashed mass ratio that is the mass ratio for the incident droplet mass to the splashed droplet mass  
786 is calculated as below which is dependent on  $u$ .

$$M_{ratio} = -27.2 + 3.15u - 0.116u^2 + 0.0014u^3 \quad (12)$$

Where,

$$u = V_{nd} \left( \frac{\rho}{\sigma} \right)^{1/4} v^{-1/8} f^{-3/8} \quad (13)$$

787 The position of the droplets can be calculated using the velocity of the droplets splashed into the  
788 domain. This helps in predicting the film flow towards the edges. The Weibull distribution for  
789 velocity is dependent on the impingement angle for the normal component. The following  
790 equations help resolve the velocity:

$$Pdf_i \left( \frac{V_{ni}}{V_{nd}} \right) = \left( \frac{b_v}{\theta_v} \left( \frac{V_{ni}}{\theta_v} \right)^{b_v-1} \right) \exp \left( - \left( \frac{V_{ni}}{\theta_v} \right)^{b_v} \right) \quad (14)$$

791 where,  $b_v = 2.1$  when  $\theta_i \leq 50^\circ$  and  $b_v = 1.10 + 0.020\theta_i$  when  $\theta_i \geq 50^\circ$ . Also,  $\theta_v = 0.158e^{0.017\theta_i} \theta_i$   
792 is the impingement angle. The splashed drop refraction angle is calculated as  $\theta_s = 65.4 + 0.266\theta_i$

$$V_{\tau i} = \frac{V_{ni}}{\tan \theta_s}; V'_{ni} = \sqrt{K} V_{ni}; V'_{\tau i} = \sqrt{K} V_{\tau i} \quad (15)$$

$$K = \frac{\frac{1}{2} m_d v_d^2 + \pi \sigma N_d d_d^2 - \frac{1}{2} m_d v_s^2}{\frac{1}{2} \sum_{i=1}^{N_{parcel}} m_i v_i^2 + \pi \sigma \sum_{i=1}^{N_{parcel}} N_i d_i^2} \quad (16)$$

793 Here,  $V_{ni}$  and  $V_{nd}$  are the splashed and incoming drop velocities. Where,  $V_s = 18 \left( \frac{\sigma}{\rho} \right)^{1/4} v^{1/8} f^{3/8}$

794 and frequency of the first drop is  $f = \frac{V_{nd}}{X_{CFD\ cell}}$

795 Finally, the splashed droplet diameter which determines number of particles in each parcel is  
796 defined below. A Weibull distribution shown below is used for the calculation of the splashed drop  
797 diameter:

$$Pdf_i \left( \frac{d_{ni}}{d_{nd}} \right) = \left( \frac{b}{\theta_w} \left( \frac{d_i}{\theta_w} \right)^{b-1} \right) \exp \left( - \left( \frac{d_i}{\theta_w} \right)^b \right) \quad (17)$$

798 where,  $b = 2.71 - (9.25 * 10^{-4})We$  and  $\theta_w = 0.210 - (7.69 * 10^{-5})We$ . Also,  $d_i$  and  $d_d$  are  
 799 splashed and incoming drop diameters, respectively. The number of particles for the  $i^{\text{th}}$  parcel is  
 800  $N_i = N_{tot}pdf_i$  and  $N_{tot}$  is the total number of splashed particles calculated by the following  
 801 equation:

$$\frac{\pi}{6} N_{tot} \sum_{i=1}^{N_{parcel}} (pdf_i d_i^3) = \frac{m_s}{m_d} m_{dd} \quad (18)$$

$$802 \quad M_{ratio} = -27.2 + 3.15u - 0.116u^2 + 0.0014u^3u = V_{nd} \left(\frac{\rho}{\sigma}\right)^{1/4} v^{-1/8} f^{-3/8} Pdf_i \left(\frac{V_{ni}}{V_{nd}}\right)$$

$$803 \quad = \left( \frac{b_v}{\theta_v} \left( \frac{V_{ni}}{V_{nd}} \right)^{b_v-1} \right) \exp \left( - \left( \frac{V_{ni}}{\theta_v} \right)^{b_v} \right) \quad V_{\tau i} = \frac{V_{ni}}{\tan \theta_s}; \quad V'_{ni} = \sqrt{K} V_{ni}; \quad V'_{\tau i}$$

$$804 \quad = \sqrt{K} V_{\tau i} K = \frac{\frac{1}{2} m_d v_d^2 + \pi \sigma N_d d_d^2 - \frac{1}{2} m_d v_s^2}{\frac{1}{2} \sum_{i=1}^{N_{parcel}} m_i v_i^2 + \pi \sigma \sum_{i=1}^{N_{parcel}} N_i d_i^2} Pdf_i \left( \frac{d_{ni}}{d_{nd}} \right)$$

$$805 \quad = \left( \frac{b}{\theta_w} \left( \frac{d_i}{d_d} \right)^{b-1} \right) \exp \left( - \left( \frac{d_i}{\theta_w} \right)^b \right) \frac{\pi}{6} N_{tot} \sum_{i=1}^{N_{parcel}} (pdf_i d_i^3) = \frac{m_s}{m_d} m_{dd}$$

$$V'_{\tau d} = \frac{5}{7} V_{\tau d} \quad (7)$$

$$V'_{nd} = \frac{5}{7} V_{nd} \quad (8)$$

$$e = 0.993 - 1.76\theta_i + 1.56\theta_i^2 - 0.49\theta_i^3 \quad (9)$$

$$\varphi = -\frac{\pi}{\beta} \ln(1 - p(1 - e^{-\beta})) \quad (10)$$

806 where  $p$  is in the  $[0,1]$  range and  $\beta$  is given by the following equation:

$$\sin \alpha = \left( \frac{e^\beta + 1}{e^\beta - 1} \right) \frac{1}{1 + (\pi/\beta)^2} \quad (11)$$

807 where  $\alpha$  is the wall inclination angle measured from wall normal.

808 **References**

- 809 1. Huang, S.; Vignolles, M.-L.; Chen, X. D.; Le Loir, Y.; Jan, G.; Schuck, P.; Jeantet, R., Spray  
810 drying of probiotics and other food-grade bacteria: A review. *Trends in food science technology*  
811 **2017**, *63*, 1-17.
- 812 2. Gharsallaoui, A.; Roudaut, G.; Chambin, O.; Voilley, A.; Saurel, R., Applications of spray-  
813 drying in microencapsulation of food ingredients: An overview. *Food research international* **2007**,  
814 *40* (9), 1107-1121.
- 815 3. Drosou, C. G.; Krokida, M. K.; Biliaderis, C. G., Encapsulation of bioactive compounds  
816 through electrospinning/electrospraying and spray drying: A comparative assessment of food-  
817 related applications. *Drying technology* **2017**, *35* (2), 139-162.
- 818 4. Singh, A.; Van den Mooter, G., Spray drying formulation of amorphous solid dispersions.  
819 *Advanced drug delivery reviews* **2016**, *100*, 27-50.
- 820 5. Broadhead, J.; Edmond Rouan, S.; Rhodes, C., The spray drying of pharmaceuticals. *Drug*  
821 *development industrial pharmacy* **1992**, *18* (11-12), 1169-1206.
- 822 6. Dugas, V.; Broutin, J.; Souteyrand, E., Droplet evaporation study applied to DNA chip  
823 manufacturing. *Langmuir* **2005**, *21* (20), 9130-9136.
- 824 7. Shariatnia, S.; Veldanda, A.; Obeidat, S.; Jarrahbashi, D.; Asadi, A., Atomization of  
825 cellulose nanocrystals aqueous suspensions in fused deposition modeling: A scalable technique  
826 to improve the strength of 3D printed polymers. *Composites Part B: Engineering* **2019**, *177*,  
827 107291.
- 828 8. Kuznetsov, I.; Greenfield, M.; Mehta, Y.; Merchan-Merchan, W.; Salkar, G.; Saveliev, A.,  
829 Increasing the solar cell power output by coating with transition metal-oxide nanorods. *Applied*  
830 *energy* **2011**, *88* (11), 4218-4221.
- 831 9. Krebs, F. C., Fabrication and processing of polymer solar cells: A review of printing and  
832 coating techniques. *Solar energy materials solar cells* **2009**, *93* (4), 394-412.
- 833 10. Giroto, C.; Rand, B. P.; Genoe, J.; Heremans, P., Exploring spray coating as a deposition  
834 technique for the fabrication of solution-processed solar cells. *Solar energy materials solar cells*  
835 **2009**, *93* (4), 454-458.
- 836 11. Zhao, D.; Liu, T.; Park, J. G.; Zhang, M.; Chen, J.-M.; Wang, B., Conductivity enhancement  
837 of aerosol-jet printed electronics by using silver nanoparticles ink with carbon nanotubes.  
838 *Microelectronic Engineering* **2012**, *96*, 71-75.
- 839 12. Paulsen, J. A.; Renn, M.; Christenson, K.; Plourde, R. In *Printing conformal electronics on*  
840 *3D structures with Aerosol Jet technology*, 2012 Future of Instrumentation International  
841 Workshop (FIW) Proceedings, IEEE: 2012; pp 1-4.
- 842 13. Phan, H. T.; Caney, N.; Marty, P.; Colasson, S.; Gavillet, J., Surface wettability control by  
843 nanocoating: the effects on pool boiling heat transfer and nucleation mechanism. *International*  
844 *Journal of Heat and Mass Transfer* **2009**, *52* (23-24), 5459-5471.
- 845 14. Matthews, S.; James, B., Review of thermal spray coating applications in the steel  
846 industry: part 1—hardware in steel making to the continuous annealing process. *Journal of*  
847 *thermal spray technology* **2010**, *19* (6), 1267-1276.
- 848 15. Moridi, A.; Hassani-Gangaraj, S. M.; Guagliano, M.; Dao, M., Cold spray coating: review  
849 of material systems and future perspectives. *Surface Engineering* **2014**, *30* (6), 369-395.
- 850 16. Barbezat, G., Advanced thermal spray technology and coating for lightweight engine  
851 blocks for the automotive industry. *Surface Coatings Technology* **2005**, *200* (5-6), 1990-1993.

- 852 17. Fauchais, P. L.; Heberlein, J. V.; Boulos, M. I., Wire arc spraying. In *Thermal Spray*  
853 *Fundamentals*, Springer: 2014; pp 577-629.
- 854 18. Gedzevicius, I.; Valiulis, A., Analysis of wire arc spraying process variables on coatings  
855 properties. *Journal of Materials Processing Technology* **2006**, *175* (1-3), 206-211.
- 856 19. Calvert, P. J. C. o. m., Inkjet printing for materials and devices. *Chemistry of materials*  
857 **2001**, *13* (10), 3299-3305.
- 858 20. Dinh, N. T.; Sowade, E.; Blaudeck, T.; Hermann, S.; Rodriguez, R. D.; Zahn, D. R.; Schulz,  
859 S. E.; Baumann, R. R.; Kanoun, O., High-resolution inkjet printing of conductive carbon nanotube  
860 twin lines utilizing evaporation-driven self-assembly. *Carbon* **2016**, *96*, 382-393.
- 861 21. Zhang, Z.; Zhu, W., Controllable fabrication of a flexible transparent metallic grid  
862 conductor based on the coffee ring effect. *Journal of Materials Chemistry C* **2014**, *2* (45), 9587-  
863 9591.
- 864 22. Bugakova, D.; Slabov, V.; Sergeeva, E.; Zhukov, M.; Vinogradov, A., Comprehensive  
865 characterization of TiO<sub>2</sub> inks and their application for inkjet printing of microstructures. *Colloids*  
866 *Surfaces A: Physicochemical Engineering Aspects* **2019**, 124146.
- 867 23. Kawakita, J.; Katanoda, H.; Watanabe, M.; Yokoyama, K.; Kuroda, S., Warm Spraying: An  
868 improved spray process to deposit novel coatings. *Surface Coatings Technology* **2008**, *202* (18),  
869 4369-4373.
- 870 24. Kuroda, S.; Kawakita, J.; Watanabe, M.; Kim, K.; Molak, R.; Katanoda, H., Current status  
871 and future prospects of warm spray technology. In *Future Development of Thermal Spray*  
872 *Coatings*, Elsevier: 2015; pp 163-206.
- 873 25. Heimann, R. B., Plasma-spray coating. *Principles Applications* **1996**, 2.
- 874 26. Cao, X.; Vassen, R.; Schwartz, S.; Jungen, W.; Tietz, F.; Stöver, D., Spray-drying of  
875 ceramics for plasma-spray coating. *Journal of the European Ceramic Society* **2000**, *20* (14-15),  
876 2433-2439.
- 877 27. Ke, D.; Vu, A. A.; Bandyopadhyay, A.; Bose, S., Compositionally graded doped  
878 hydroxyapatite coating on titanium using laser and plasma spray deposition for bone implants.  
879 *Acta biomaterialia* **2019**, *84*, 414-423.
- 880 28. Watanabe, T.; Sato, T.; Nezu, A., Electrode phenomena investigation of wire arc spraying  
881 for preparation of Ti-Al intermetallic compounds. *Thin Solid Films* **2002**, *407* (1-2), 98-103.
- 882 29. Pawlowski, L., *The science and engineering of thermal spray coatings*. John Wiley & Sons:  
883 2008.
- 884 30. Fauchais, P.; Vardelle, M.; Vardelle, A.; Goutier, S., What do we know, what are the  
885 current limitations of suspension plasma spraying? *Journal of Thermal Spray Technology* **2015**,  
886 *24* (7), 1120-1129.
- 887 31. Davis, J. R., *Handbook of thermal spray technology*. ASM international: 2004.
- 888 32. Fotovvati, B.; Namdari, N.; Dehghanhadikolaee, A., On coating techniques for surface  
889 protection: a review. *Journal of Manufacturing Materials Processing* **2019**, *3* (1), 28.
- 890 33. Le, H. P., Progress and trends in ink-jet printing technology. *ournal of Imaging Science*  
891 *Technology* **1998**, *42* (1), 49-62.
- 892 34. Carter, J. C.; Alvis, R. M.; Brown, S. B.; Langry, K. C.; Wilson, T. S.; McBride, M. T.; Myrick,  
893 M.; Cox, W. R.; Grove, M. E.; Colston, B. W., Fabricating optical fiber imaging sensors using inkjet  
894 printing technology: A pH sensor proof-of-concept. *Biosensors and Bioelectronics* **2006**, *21* (7),  
895 1359-1364.

- 896 35. Chang, S. C.; Liu, J.; Bharathan, J.; Yang, Y.; Onohara, J.; Kido, J., Multicolor organic light-  
897 emitting diodes processed by hybrid inkjet printing. *Advanced Materials* **1999**, *11* (9), 734-737.
- 898 36. Han, S.-Y.; Lee, D.-H.; Herman, G. S.; Chang, C.-H., Inkjet-printed high mobility  
899 transparent-oxide semiconductors. *Journal of Display Technology* **2009**, *5* (12), 520-524.
- 900 37. Haverinen, H. M.; Myllylä, R. A.; Jabbour, G. E., Inkjet printing of light emitting quantum  
901 dots. *Applied Physics Letters* **2009**, *94* (7), 073108.
- 902 38. Haverinen, H. M.; Myllylä, R. A.; Jabbour, G. E., Inkjet printed RGB quantum dot-hybrid  
903 LED. *Journal of display technology* **2010**, *6* (3), 87-89.
- 904 39. Kawase, T.; Shimoda, T.; Newsome, C.; Siringhaus, H.; Friend, R. H., Inkjet printing of  
905 polymer thin film transistors. *Thin solid films* **2003**, *438*, 279-287.
- 906 40. Hedges, M.; Marin, A. B. In *3D Aerosol jet printing-Adding electronics functionality to*  
907 *RP/RM*, DDMC 2012 conference, 2012; pp 14-15.3.
- 908 41. Ebert, J.; Özkol, E.; Zeichner, A.; Uibel, K.; Weiss, Ö.; Koops, U.; Telle, R.; Fischer, H.,  
909 Direct inkjet printing of dental prostheses made of zirconia. *Journal of dental research* **2009**, *88*  
910 (7), 673-676.
- 911 42. Cui, X.; Boland, T.; DD'Lima, D.; K Lotz, M., Thermal inkjet printing in tissue engineering  
912 and regenerative medicine. *Recent patents on drug delivery formulation* **2012**, *6* (2), 149-155.
- 913 43. Boland, T.; Xu, T.; Damon, B.; Cui, X., Application of inkjet printing to tissue engineering.  
914 *Biotechnology Journal: Healthcare Nutrition Technology* **2006**, *1* (9), 910-917.
- 915 44. Cummins, G.; Desmulliez, M. P., Inkjet printing of conductive materials: a review. *Circuit*  
916 *world* **2012**.
- 917 45. Derby, B., Inkjet printing ceramics: From drops to solid. *Journal of the European Ceramic*  
918 *Society* **2011**, *31* (14), 2543-2550.
- 919 46. Lee, Y.; Choi, J.-r.; Lee, K. J.; Stott, N. E.; Kim, D., Large-scale synthesis of copper  
920 nanoparticles by chemically controlled reduction for applications of inkjet-printed electronics.  
921 *Nanotechnology* **2008**, *19* (41), 415604.
- 922 47. Magdassi, S., In *The Chemistry of Inkjet Inks*; Magdassi, S., Ed. World Scientific Publishing  
923 Co. Pte. Ltd.: Hackensack, NJ: 2010.
- 924 48. Deegan, R. D.; Bakajin, O.; Dupont, T. F.; Huber, G.; Nagel, S. R.; Witten, T. A. J. N.,  
925 Capillary flow as the cause of ring stains from dried liquid drops. *Nature* **1997**, *389* (6653), 827.
- 926 49. Yunker, P. J.; Still, T.; Lohr, M. A.; Yodh, A., Suppression of the coffee-ring effect by shape-  
927 dependent capillary interactions. *Nature* **2011**, *476* (7360), 308-311.
- 928 50. Anyfantakis, M.; Geng, Z.; Morel, M.; Rudiuk, S.; Baigl, D. J. L., Modulation of the coffee-  
929 ring effect in particle/surfactant mixtures: the importance of particle-interface interactions.  
930 *Langmuir* **2015**, *31* (14), 4113-4120.
- 931 51. Nguyen, V. X.; Stebe, K. J., Patterning of small particles by a surfactant-enhanced  
932 Marangoni-Bénard instability. *Physical Review Letters* **2002**, *88* (16), 164501.
- 933 52. Seo, C.; Jang, D.; Chae, J.; Shin, S., Altering the coffee-ring effect by adding a surfactant-  
934 like viscous polymer solution. *Scientific reports* **2017**, *7* (1), 500.
- 935 53. Dicuango, M.; Dash, S.; Weibel, J. A.; Garimella, S. V., Effect of superhydrophobic surface  
936 morphology on evaporative deposition patterns. *Applied Physics Letters* **2014**, *104* (20), 201604.
- 937 54. Cui, L.; Zhang, J.; Zhang, X.; Li, Y.; Wang, Z.; Gao, H.; Wang, T.; Zhu, S.; Yu, H.; Yang,  
938 B., Avoiding coffee ring structure based on hydrophobic silicon pillar arrays during single-drop  
939 evaporation. *Soft Matter* **2012**, *8* (40), 10448-10456.

- 940 55. Mampallil, D.; Eral, H.; Van Den Ende, D.; Mugele, F., Control of evaporating complex  
941 fluids through electrowetting. *Soft Matter* **2012**, *8* (41), 10614-10617.
- 942 56. Mampallil, D.; Reboud, J.; Wilson, R.; Wylie, D.; Klug, D. R.; Cooper, J. M., Acoustic  
943 suppression of the coffee-ring effect. *Soft matter* **2015**, *11* (36), 7207-7213.
- 944 57. Mampallil, D.; Eral, H. B., A review on suppression and utilization of the coffee-ring effect.  
945 *Advances in colloid interface science* **2018**, *252*, 38-54.
- 946 58. Castrejon-Pita, J. R.; Baxter, W.; Morgan, J.; Temple, S.; Martin, G.; Hutchings, I. J. A.;  
947 sprays, Future, opportunities and challenges of inkjet technologies. *Atomization and sprays* **2013**,  
948 *23* (6).
- 949 59. Seifert, T.; Sowade, E.; Roscher, F.; Wiemer, M.; Gessner, T.; Baumann, R. R., Additive  
950 manufacturing technologies compared: morphology of deposits of silver ink using inkjet and  
951 aerosol jet printing. *Industrial Engineering Chemistry Research* **2015**, *54* (2), 769-779.
- 952 60. Mooney, J. B.; Radding, S. B., Spray pyrolysis processing. *Annual review of materials*  
953 *science* **1982**, *12* (1), 81-101.
- 954 61. Vehring, R.; Foss, W. R.; Lechuga-Ballesteros, D., Particle formation in spray drying. *ournal*  
955 *of Aerosol Science* **2007**, *38* (7), 728-746.
- 956 62. Sollohub, K.; Cal, K., Spray drying technique: II. Current applications in pharmaceutical  
957 technology. *Journal of pharmaceutical sciences* **2010**, *99* (2), 587-597.
- 958 63. Qi, S.; Craig, D., Recent developments in micro-and nanofabrication techniques for the  
959 preparation of amorphous pharmaceutical dosage forms. *Advanced Drug Delivery Reviews* **2016**,  
960 *100*, 67-84.
- 961 64. Raula, J.; Eerikäinen, H.; Kauppinen, E. I., Influence of the solvent composition on the  
962 aerosol synthesis of pharmaceutical polymer nanoparticles. *International journal of*  
963 *pharmaceutics* **2004**, *284* (1-2), 13-21.
- 964 65. Haque, E.; Shariatnia, S.; Jeong, T.-J.; Jarrahbashi, D.; Asadi, A.; Harris, T.; Moon, R. J.;  
965 Kalaitzidou, K., Scalable coating methods for enhancing glass fiber–epoxy interactions with  
966 cellulose nanocrystals. *Cellulose* **2021**, 1-16.
- 967 66. Wei, Y.; Huang, Y.-H.; Cheng, K.-C.; Song, Y.-L., Investigations of the Influences of  
968 Processing Conditions on the Properties of Spray Dried Chitosan-Tripolyphosphate Particles  
969 loaded with theophylline. *Scientific Reports* **2020**, *10* (1), 1-12.
- 970 67. Wilkinson, N.; Smith, M.; Kay, R.; Harris, R., A review of aerosol jet printing—a non-  
971 traditional hybrid process for micro-manufacturing. *The International Journal of Advanced*  
972 *Manufacturing Technology* **2019**, *105* (11), 4599-4619.
- 973 68. Lu, S.; Zheng, J.; Cardenas, J. A.; Williams, N. X.; Lin, Y.-C.; Franklin, A. D., Uniform and  
974 Stable Aerosol Jet Printing of Carbon Nanotube Thin-Film Transistors by Ink Temperature Control.  
975 *ACS Applied Materials Interfaces* **2020**, *12* (38), 43083-43089.
- 976 69. Secor, E. B., Principles of aerosol jet printing. *Flexible and Printed Electronics* **2018**, *3* (3),  
977 035002.
- 978 70. Mette, A.; Richter, P.; Hörteis, M.; Glunz, S., Metal aerosol jet printing for solar cell  
979 metallization. *Progress in Photovoltaics: Research Applications* **2007**, *15* (7), 621-627.
- 980 71. Azarova, N. A.; Owen, J. W.; McLellan, C. A.; Grimminger, M. A.; Chapman, E. K.;  
981 Anthony, J. E.; Jurchescu, O. D., Fabrication of organic thin-film transistors by spray-deposition  
982 for low-cost, large-area electronics. *Organic Electronics* **2010**, *11* (12), 1960-1965.

- 983 72. Sarobol, P.; Cook, A.; Clem, P. G.; Keicher, D.; Hirschfeld, D.; Hall, A. C.; Bell, N. S.,  
984 Additive manufacturing of hybrid circuits. *Annual Review of Materials Research* **2016**, *46*, 41-62.
- 985 73. Jabari, E.; Toyserkani, E. J. C., Micro-scale aerosol-jet printing of graphene interconnects.  
986 *Carbon* **2015**, *91*, 321-329.
- 987 74. Goth, C.; Putzo, S.; Franke, J. In *Aerosol Jet printing on rapid prototyping materials for*  
988 *fine pitch electronic applications*, 2011 IEEE 61st Electronic Components and Technology  
989 Conference (ECTC), IEEE: 2011; pp 1211-1216.
- 990 75. Mahajan, A.; Frisbie, C. D.; Francis, L. F., Optimization of aerosol jet printing for high-  
991 resolution, high-aspect ratio silver lines. *ACS applied materials interfaces* **2013**, *5* (11), 4856-4864.
- 992 76. Reverchon, E., Supercritical-assisted atomization to produce micro-and/or nanoparticles  
993 of controlled size and distribution. *Industrial engineering & chemistry research* **2002**, *41* (10),  
994 2405-2411.
- 995 77. Shariati, A.; Peters, C. J., Recent developments in particle design using supercritical fluids.  
996 *Current Opinion in Solid State Materials Science* **2003**, *7* (4-5), 371-383.
- 997 78. Tom, J. W.; Debenedetti, P. G., Particle formation with supercritical fluids—a review.  
998 *Journal of Aerosol Science* **1991**, *22* (5), 555-584.
- 999 79. Reverchon, E., Process for the production of micro and/or nano particles. Google Patents:  
1000 2007.
- 1001 80. Diamond, L. W.; Akinfiyev, N. N., Solubility of CO<sub>2</sub> in water from– 1.5 to 100 C and from 0.1  
1002 to 100 MPa: evaluation of literature data and thermodynamic modelling. *Fluid phase equilibria*  
1003 **2003**, *208* (1-2), 265-290.
- 1004 81. Aguiar-Ricardo, A., Building dry powder formulations using supercritical CO<sub>2</sub> spray drying.  
1005 *Current Opinion in Green Sustainable Chemistry* **2017**, *5*, 12-16.
- 1006 82. Nunes, A. V.; Duarte, C. M., Dense CO<sub>2</sub> as a solute, co-solute or co-solvent in particle  
1007 formation processes: a review. *Materials* **2011**, *4* (11), 2017-2041.
- 1008 83. Costa, C.; Casimiro, T.; Aguiar-Ricardo, A., Optimization of supercritical CO<sub>2</sub>-assisted  
1009 atomization: Phase behavior and design of experiments. *Journal of Chemical Engineering Data*  
1010 **2018**, *63* (4), 885-896.
- 1011 84. Della Porta, G.; De Vittori, C.; Reverchon, E., Supercritical assisted atomization: a novel  
1012 technology for microparticles preparation of an asthma-controlling drug. *Aaps Pharmscitech*  
1013 **2005**, *6* (3), E421-E428.
- 1014 85. Shariatnia, S.; Asadi, A.; Jarrahbashi, D., Experimental analysis of supercritical-assisted  
1015 atomization. *Physics of Fluids* **2021**, *33* (1), 013314.
- 1016 86. Palaganas, N. B.; Mangadlao, J. D.; de Leon, A. C. C.; Palaganas, J. O.; Pangilinan, K. D.;  
1017 Lee, Y. J.; Advincula, R. C., 3D printing of photocurable cellulose nanocrystal composite for  
1018 fabrication of complex architectures via stereolithography. *ACS applied materials interfaces*  
1019 **2017**, *9* (39), 34314-34324.
- 1020 87. Tang, J.; Sisler, J.; Grishkewich, N.; Tam, K. C., Functionalization of cellulose nanocrystals  
1021 for advanced applications. *Journal of colloid interface science* **2017**, *494*, 397-409.
- 1022 88. Shariatnia, S.; Kumar, A. V.; Kaynan, O.; Asadi, A., Hybrid Cellulose Nanocrystals-Bonded  
1023 Carbon Nanotubes/Carbon Fiber Polymer Composites for Structural Applications. *ACS Applied*  
1024 *Nano Materials* **2020**.
- 1025 89. Roman, M.; Dong, S.; Hirani, A.; Lee, Y. W., Cellulose nanocrystals for drug delivery. ACS  
1026 Publications: 2009.

- 1027 90. Grishkewich, N.; Mohammed, N.; Tang, J.; Tam, K. C., Recent advances in the application  
1028 of cellulose nanocrystals. *Current Opinion in Colloid Interface Science* **2017**, *29*, 32-45.
- 1029 91. Mariano, M.; El Kissi, N.; Dufresne, A., Cellulose nanocrystals and related  
1030 nanocomposites: review of some properties and challenges. *Journal of Polymer Science Part B:*  
1031 *Polymer Physics* **2014**, *52* (12), 791-806.
- 1032 92. Moon, R. J.; Martini, A.; Nairn, J.; Simonsen, J.; Youngblood, J., Cellulose nanomaterials  
1033 review: structure, properties and nanocomposites. *Chemical Society Reviews* **2011**, *40* (7), 3941-  
1034 3994.
- 1035 93. Parker, R. M.; Frka-Petesic, B.; Guidetti, G.; Kamita, G.; Consani, G.; Abell, C.; Vignolini,  
1036 S., Hierarchical self-assembly of cellulose nanocrystals in a confined geometry. *ACS nano* **2016**,  
1037 *10* (9), 8443-8449.
- 1038 94. Mu, X.; Gray, D. G., Droplets of cellulose nanocrystal suspensions on drying give iridescent  
1039 3-D “coffee-stain” rings. *Cellulose* **2015**, *22* (2), 1103-1107.
- 1040 95. Parker, R. M.; Guidetti, G.; Williams, C. A.; Zhao, T.; Narkevicius, A.; Vignolini, S.; Frka-  
1041 Petesic, B., The Self-Assembly of Cellulose Nanocrystals: Hierarchical Design of Visual  
1042 Appearance. *Advanced Materials* **2018**, *30* (19), 1704477.
- 1043 96. Shopsowitz, K. E.; Qi, H.; Hamad, W. Y.; MacLachlan, M. J., Free-standing mesoporous  
1044 silica films with tunable chiral nematic structures. *Nature* **2010**, *468* (7322), 422-425.
- 1045 97. Gu, M.; Jiang, C.; Liu, D.; Prempeh, N.; Smalyukh, I. I., Cellulose nanocrystal/poly  
1046 (ethylene glycol) composite as an iridescent coating on polymer substrates: structure-color and  
1047 interface adhesion. *ACS applied materials interfaces* **2016**, *8* (47), 32565-32573.
- 1048 98. Andrews, S.; Nover, D.; Reuter, J.; Schladow, S., Limitations of laser diffraction for  
1049 measuring fine particles in oligotrophic systems: Pitfalls and potential solutions. *Water Resources*  
1050 *Research* **2011**, *47* (5).
- 1051 99. Weller, H. G.; Tabor, G.; Jasak, H.; Fureby, C., A tensorial approach to computational  
1052 continuum mechanics using object-oriented techniques. *Computers in physics* **1998**, *12* (6), 620-  
1053 631.
- 1054 100. Tsang, C.-W.; Trujillo, M. F.; Rutland, C. J., Large-eddy simulation of shear flows and high-  
1055 speed vaporizing liquid fuel sprays. *Computers and Fluids* **2014**, *105*, 262-279.
- 1056 101. Mishra, R.; Rutland, C. *Evaluating Surface Film Models for Multi-Dimensional Modeling of*  
1057 *Spray-Wall Interaction*; 0148-7191; SAE Technical Paper: 2019.
- 1058 102. Stanton, D. W.; Rutland, C. J., Modeling fuel film formation and wall interaction in diesel  
1059 engines. *SAE transactions* **1996**, 808-824.
- 1060 103. Markt, D. P.; Torelli, R.; Pathak, A.; Raessi, M.; Som, S.; Scarcelli, R.; Lee, S.-Y.; Naber,  
1061 J. *Using a DNS framework to test a splashed mass sub-model for Lagrangian spray simulations*;  
1062 0148-7191; SAE Technical Paper: 2018.
- 1063 104. Reitz, R. D., Modeling Atomization Processes in High-Pressure Vaporizing Sprays.  
1064 *Atomization and Spray Technology* **1987**, Vol 3, 309-337.
- 1065 105. Zuo B., G. A. M., Rutland C. J., Studies of Superheated Fuel Spray Structures and  
1066 Vaporization in GDI Engines. *International Journal of Engine Research* **2000**, Vol. 1(4), 321-336.
- 1067 106. Ranz, W. E., Marshall, W.R, Evaporation from drops. *Chem. Eng. Prog* **1952**, *48*, 141-146.
- 1068 107. Jarrahbashi, D.; Kim, S.; Genzale, C. L., Simulation of Combustion Recession After End-of-  
1069 Injection at Diesel Engine Conditions. *Journal of Engineering for Gas Turbines and Power* **2017**,  
1070 *139* (10), 102804-102804-8.

- 1071 108. Jarrahbashi, D.; Kim, S.; Knox, B. W.; Genzale, C. L., Computational analysis of end-of-  
1072 injection transients and combustion recession. *International Journal of Engine Research* **2017**, *18*  
1073 (10), 1088-1110.
- 1074 109. Stanton D., R. C., Modeling Fuel Film Formation and Wall Interaction in Diesel Engines.  
1075 *SAE Technical Paper* **1996**, (960628), 10.4271/960628.
- 1076 110. W., W., A statistical distribution function of wide applicability. *J Appl Mech* **1951**, *18*, 293–  
1077 297.
- 1078 111. Jarrahbashi, D.; Sirignano, W. A., Vorticity dynamics for transient high-pressure liquid  
1079 injection. *Physics of Fluids* **2014**, *26* (10), 101304.
- 1080 112. Jarrahbashi, D.; Sirignano, W. A.; Popov, P. P.; Hussain, F., Early spray development at  
1081 high gas density: hole, ligament and bridge formations. *Journal of Fluid Mechanics* **2016**, *792*,  
1082 186-231.
- 1083 113. Diamond, L. W.; Akinfiev, N. N., Solubility of CO<sub>2</sub> in water from –1.5 to 100 °C and from  
1084 0.1 to 100 MPa: evaluation of literature data and thermodynamic modelling. *Fluid Phase*  
1085 *Equilibria* **2003**, *208* (1-2), 265-290.
- 1086 114. Bachu, S.; Bennion, D. B., Interfacial tension between CO<sub>2</sub>, freshwater, and brine in the  
1087 range of pressure from (2 to 27) MPa, temperature from (20 to 125) C, and water salinity from (0  
1088 to 334 000) mg·L<sup>-1</sup>. *Journal of Chemical Engineering Data* **2009**, *54* (3), 765-775.
- 1089 115. Tewes, F.; Boury, F., Formation and Rheological Properties of the Supercritical CO<sub>2</sub>–  
1090 Water Pure Interface. *The Journal of Physical Chemistry B* **2005**, *109* (9), 3990-3997.
- 1091 116. Bouse, L.; Kirk, I.; Bode, L., Effect of spray mixture on droplet size. *Transactions of the*  
1092 *ASAE* **1990**, *33* (3), 783-0788.
- 1093 117. Dayal, P.; Shaik, M. S.; Singh, M., Evaluation of different parameters that affect droplet-  
1094 size distribution from nasal sprays using the Malvern Spraytec®. *Journal of pharmaceutical*  
1095 *sciences* **2004**, *93* (7), 1725-1742.
- 1096 118. Govor, L.; Reiter, G.; Bauer, G.; Parisi, J., Nanoparticle ring formation in evaporating  
1097 micron-size droplets. *Applied physics letters* **2004**, *84* (23), 4774-4776.
- 1098 119. Lu, G.; Hu, H.; Duan, Y.; Sun, Y., Wetting kinetics of water nano-droplet containing non-  
1099 surfactant nanoparticles: A molecular dynamics study. *Applied Physics Letters* **2013**, *103* (25),  
1100 253104.
- 1101 120. Vehring, R., Pharmaceutical particle engineering via spray drying. *Pharmaceutical*  
1102 *research* **2008**, *25* (5), 999-1022.
- 1103 121. Wei, Y., Effect of particles on evaporation of droplet containing particles. **2015**.
- 1104 122. Mampallil, D.; Eral, H. B., A review on suppression and utilization of the coffee-ring effect.  
1105 *Adv Colloid Interface Sci* **2018**, *252*, 38-54.
- 1106 123. Hu, H.; Larson, R. G., Evaporation of a sessile droplet on a substrate. *The Journal of*  
1107 *Physical Chemistry B* **2002**, *106* (6), 1334-1344.
- 1108 124. Nguyen, T. A.; Nguyen, A. V., Increased evaporation kinetics of sessile droplets by using  
1109 nanoparticles. *Langmuir* **2012**, *28* (49), 16725-16728.
- 1110 125. Hu, H.; Larson, R. G., Analysis of the microfluid flow in an evaporating sessile droplet.  
1111 *Langmuir* **2005**, *21* (9), 3963-3971.
- 1112 126. Weast, R.; Astle, M. J. C., Boca Raton, Fla, CRC Handbook of chemistry and physics 62nd  
1113 ed. **1981**.

1114 127. Van Rie, J.; Schütz, C.; Gençer, A.; Lombardo, S.; Gasser, U.; Kumar, S.; Salazar-Alvarez,  
1115 G. n.; Kang, K.; Thielemans, W., Anisotropic diffusion and phase behavior of cellulose nanocrystal  
1116 suspensions. *Langmuir* **2019**, *35* (6), 2289-2302.  
1117